Net Radiative Effects of Dust in Tropical North Atlantic Based on Integrated Satellite Observations and In Situ Measurements

Qianqian Song[1,2], Zhibo Zhang[1,2]*, Hongbin Yu[3], Seiji Kato[4], Ping Yang[5], Peter Colarco[3], Lorraine A. Remer[2], Claire L. Ryder[6]

1. Physics Department, University of Maryland Baltimore County
2. Joint Center for Earth Systems Technology, University of Maryland Baltimore County
3. NASA Goddard Space Flight Center
4. NASA Langley Research Center.
5. Dept. of Atmospheric Sciences, Texas A&M University
6. Department of Meteorology, University of Reading, RG6 6BB, UK.

Send Correspondence to:
Dr. Zhibo Zhang
Email: zhibo.zhang@umbc.edu

27   **Abstract**
28   In this study, we integrate the recent in situ measurements with satellite retrievals of dust

29   physical and radiative properties to quantify the dust direct radiative effects on the shortwave (SW)

30   and longwave (LW) radiation (denoted as DRE_{SW} and DRE_{LW}, respectively) in the tropical North

31   Atlantic during summer months from 2007 to 2010.   Through linear regression of CERES

32   measured top-of-atmosphere (TOA) flux versus satellite aerosol optical depth (AOD) retrievals,

33   we estimate the instantaneous DRE_{SW} efficiency at the TOA to be -49.7 ± 7.1 W/m^2/AOD and $-$

34   36.5 ± 4.8 W/m^2/AOD based on AOD from MODIS and CALIOP, respectively. We then perform

35   various sensitivity studies based on recent measurements of dust particle size distribution (PSD),

36   refractive index, and particle shape distribution to determine how the dust microphysical and

37   optical properties affect DRE estimates and its agreement with abovementioned satellite-derived

38   DREs. Our analysis shows that a good agreement with the observation-based estimates of

39   instantaneous DRE_{SW} and DRE_{LW} can be achieved through a combination of recently observed

40   PSD with substantial presence of coarse particles, a less absorptive SW refractive index, and

41   spheroid shapes. Based on this optimal combination of dust physical properties we further estimate

42   the diurnal mean dust DRE_{SW} in the region of -10 W/m^2 at TOA and -26 W/m^2 at surface,

43   respectively, of which ~30% is canceled out by the positive DRE_{LW}. This yields a net DRE of

44   about -6.9 W/m^2 and -18.3 W/m^2 at TOA and surface, respectively. Our study suggests that the

45   LW flux contains useful information of dust particle size, which could be used together with SW

46   observation to achieve more holistic understanding of the dust radiative effect.

47

48

1. Introduction

Mineral dust is the most abundant atmospheric aerosol component in terms of dry mass [*Choobari et al.,* 2014, *Textor et al.,* 2006]. The Sahara is the largest source of atmospheric dust aerosols, with an estimated emission of 670 Mt yr^{-1} [*Rajot et al.,* 2008, *Washington et al.,* 2003]. African dust from Sahara is regularly lifted by strong near-surface winds and transported westwards within the Saharan Air Layer (SAL) over to the tropical North Atlantic during northern summer [*Cuesta et al.,* 2009, *Karyampudi et al.,* 1999]. During the transport, dust aerosols can scatter and absorb both shortwave solar (referred to as "SW") and longwave thermal infrared (referred to as "LW") radiation, and thereby influence Earth's energy budget [*McCormick et al.,* 1967, *Tegen et al.,* 1996, *Yu et al.,* 2006] . This is known as the direct radiative effect (DRE) of dust, which can have a significant influence on the global energy balance [*Boucher et al.* 2013], as well as regional weather and climate [e.g., *Miller and Tegen* 1998, *Evan et al.* 2006, *Lau and Kim* 2007]. Therefore, it is important to quantify dust DREs as accurate as possible. Moreover, mineral dusts can also influence the life cycle and properties of clouds, by altering thermal structure of the atmosphere (known as semi-direct effects) [*Ackerman et al.,* 2000, *Hansen et al.,* 1997, *Koren et al.,* 2004], and by acting as cloud condensation nuclei and ice nuclei (known as indirect effects) [*Albrecht,* 1989, *Rosenfeld et al.,* 1998, *Twomey,* 1977] . In addition, when African dust aerosols are deposited into Atlantic Ocean and Amazon Basin, they supply essential nutrients for the marine and rainforest ecosystems [*Yu et al., 2015*], which has important implications for the biogeochemical cycles [*Jickells et al.,* 2005]. In this study, we focus on the quantification of dust direct radiative effect on both SW and LW radiation.

Substantial effort has been made to understand and quantify the DRE of mineral dust since the 1980s [*Carlson et al.,* 1980, *Cess,* 1985, *Liao et al.,* 1998, *Ramaswamy et al.,* 1985]. Most

72 studies have focused on the SW DRE (DRE_{SW}) of mineral dust under clear-sky (cloud free)

73 conditions [*Myhre et al.,* 2003, *Tegen et al.,* 1996, *Yu et al.,* 2006] . Through scattering and

74 absorption, dust aerosols reduce the amount of solar radiation reaching the surface, inducing a

75 negative (cooling) effect at the surface. The DRE_{SW} of dust at the top of the atmosphere (TOA)

76 depends also strongly on the albedo of the underlying surface [*Keil et al.,* 2003, *Yu et al.,* 2006].

77 Over a dark surface, the scattering effect of dust dominates, it leads to a negative DRE at TOA that

78 cools the climate system [*Myhre et al.,* 2003, *Tegen et al.,* 1996] . In contrast, high reflectance of

79 a bright surface enhances the absorption by dust aerosols and could yield a positive dust DRE_{SW}

80 (warming effect on the climate system) at TOA when the surface albedo exceeds a critical value

81 [*Zhang et al. 2016, Xu et al., 2017*]. Different from other aerosol types (e.g., smoke and sulfate

82 aerosols), dust aerosols are large enough to have significant LW direct radiative effect (DRE_{LW})

83 [*Sokolik et al.,* 1999, *Sokolik et al.,* 1998]. Lofted dust aerosols absorb the LW radiation from the

84 warm surface and re-emit the LW radiation usually at lower temperature, thereby reducing the

85 outgoing LW radiation and leading to a positive DRE at TOA that tends to warm the climate

86 system. At the same time, they emit the LW radiation downward that generates a warming effect

87 at the surface. The dust LW effect depends strongly on surface emissivity [*Yang et al.,* 2009] and

88 the vertical profile of atmosphere temperature. The net radiative effect (DRE_{net}) of dust is the

89 summation of its DRE_{SW} and DRE_{LW}. Note that DRE_{SW} only acts during daytime, whereas DRE_{LW}

90 operates during both day and night.

91   Quantification of the DRE_{SW} and DRE_{LW} of dust remains challenging and there is a large

92 range of estimates in the literature. Take the Tropical Atlantic for example. Yu et al. [*2006*] found

93 that the seasonal (JJA) average clear-sky aerosol DRE_{SW} at TOA in this region varies from -5.7

94 W/m^2 to -12.8 W/m^2 based on observations and from -3.7 W/m^2 to -10.4 W/m^2 based on model

95　simulations. An important reason is that dust DRE depends on many factors, including both the

96　microphysical (e.g., dust particle size and shape) and optical (e.g., refractive index) properties, as

97　well as the surface and atmospheric properties (e.g., surface reflectance and temperature,

98　atmospheric absorption). Sokolik et al. [1998] showed that for the sub-micron dust particles, the

99　DRE_{SW} is dominant and DRE_{LW} is negligible, whereas for super-micron dust particles, DRE_{LW} is

100　more important [*Sokolik et al.,* 1996, *Sokolik et al.,* 1999]. Therefore, an accurate measurement of

101　the particle size distribution (PSD) is highly important for estimating the DRE of dust. However,

102　dust PSDs are highly variable and difficult to measure or retrieve, and, as a result, the observations

103　of dust PSD are usually subjected to large uncertainties [see Mahowald et al., 2014 and references

104　therein]. PSD inferred from AERONET observations [Dubovik et al., 2006] relies on observations

105　at shortwave channels, which could bias the dust size low. In fact, more and more observations are

106　emerging to suggest that dust PSD even in regions far from source regions contains substantial

107　fraction of coarse particles. Based on the airborne in-situ measurement of dust PSD in Caribbean

108　Basin from the Puerto Rico Dust Experiment (PRIDE) campaign, Maring et al. [2003] noted that

109　dust particles appear to settle more slowly than expected from the widely used Stokes gravitational

110　settling model. Similarly, recent measurements from the latest Fennec project [*Ryder et al.,* 2013b]

111　and the Saharan Aerosol Long-range Transport and Aerosol-Cloud-interaction Experiment

112　(SALTRACE) [*Weinzierl et al.,* 2017] all suggest that transported dust aerosols in the SAL are

113　significantly coarser than expected based on the Stokes gravitational deposition. Such unexpected

114　existence of coarse particles has important implications for understanding the DRE of dust. In a

115　case of significant fraction of coarse particles, the warming effect on LW radiation (positive)

116　DRE_{LW} would partly cancel the DRE_{SW} leading to a less negative or even positive DRE_{net}. Most

117　recently, Kok et al. [2017] argue that most of the current global climate models tend to

118   underestimate the size of dust particles and therefore overestimate the cooling effects of dust. Their

119   estimate of the global mean dust DRE_{net} is between -0.48 and $+0.20$ W m^{-2}, which includes the

120   possibility that dust causes a net warming of the planet.

121   In addition to dust particle size, particle shape and refractive index also have significant

122   influence on dust DRE. Dust particles are generally nonspherical in shape, which make their

123   single-scattering properties (i.e., extinction efficiency, single-scattering albedo and scattering

124   phase matrix) fundamentally different from those based on spherical models. A few dust particle

125   shape models have been developed [*Dubovik et al.,* 2006, *Kandler et al.,* 2009], which have been

126   increasingly used in aerosol remote sensing and modeling [*Levy et al.,* 2007]. Räisänen et al. [2013]

127   found that replacing the spherical dust models in a GCM with nonspherical model leads to

128   negligible changes in the DRE of dust at TOA. However, a recent GCM-based study by Colarco

129   et al. [2014] suggests that the influence of nonsphericity on dust DRE can be significant at surface

130   and within the atmosphere, depending on the refractive index of dust. Similarly, Kok et al. [2017]

131   argue that a spherical model significantly underestimates the extinction of dust, leading to errors

132   in estimate of dust DRE.

133   Over the past few decades, substantial efforts have been made to measure the spectral

134   refractive index of dust, mostly limited to the SW spectral range [*Balkanski et al.,* 2007, *Dubovik*

135   *et al.,* 2002, *Dubovik et al.,* 2006, *Formenti et al.,* 2011, *Hess et al.,* 1998, *Levoni et al.,* 1997].

136   The current widely-used LW refractive index of dust was measured using rather old techniques in

137   the 1970s and 1980s [e.g., Volz 1972, 1973, Fouquart et al. 1987]. Recently, Di Biagio et al. [2014,

138   2017] compiled a comprehensive dust aerosol refractive index database in the LW spectrum

139   ranging from 3 to 15 µm, based on 19 natural samples from 8 dust regions over the globe. This

140   database is the first one as far as we know to document the regional differences in dust LW

141   refractive index due to the regional characteristics of dust chemical composition. We also call

142   special attention to a newly developed database of Saharan and Asian dust [Stegmann and Yang,

143   2017].

144   Satellite observations have long become indispensable for studying the dust aerosols. In

145   particular, the combination of passive (e.g., MODIS and CERES) and active (e.g., CALIPSO)

146   sensors on board of NASA's A-Train satellite constellation provides unprecedented data to study

147   dust aerosols, from long range transport [e.g., *Liu et al. 2008, Yu et al. 2015*] to dust DRE [e.g.,

148   *Yu et al. 2006, Zhang et al. 2016*]. As A-Train observations become mature, substantial efforts

149   have been made to collocate and fuse the observations from different sensors to make the use of

150   A-Train observations easier for the users. A prominent example is the CERES- CALIPSO-

151   CloudSat -MODIS (CCCM) product developed by Kato et al. [2011], which has become a popular

152   dataset for studying the radiative effects of clouds and aerosols and for evaluating GCMs.

153   The present study is inspired and motivated by the latest measurements of the

154   microphysical and optical properties of dust, namely the in-situ dust PSD from the Fennec field

155   campaign [Ryder et al. 2013a, 2013b] and the dust LW refractive index from Di Biagio [2014,

156   2017], as well as the recent studies (e.g., Kok et al.[2017]) suggesting that cooling effects of dust

157   is overestimated in most climate models due to the underestimation of dust size. The study is

158   carried out in three steps, each with a distinct objective. First, we attempt to derive a set of

159   observation-based *instantaneous* dust DRE_{SW} and DRE_{LW} for the tropical North Atlantic based on

160   the A-Train satellite observations reported in the CCCM product, without imposing any

161   assumptions on dust size, shape or refractive index. Here, the instantaneous dust DRE represents

162   dust DRE derived under the conditions (e.g., solar position, atmospheric condition) at the measured

163   or computed time to distinguish from the diurnally averaged DRE in Section 4. Then, we perform

164   multiple sets of radiative transfer computations of the *instantaneous* dust DRE in the North

165   Atlantic region based on the same dust extinction profiles from CCCM in combination with

166   different dust physical and optical properties. The objective is to understand the sensitivity of dust

167   DRE_{SW} and DRE_{LW} to the PSD, nonsphericity, and refractive index of dust and to obtain a set of

168   dust properties that yield the best agreement with satellite flux observations (e.g., CERES). In the

169   third step, we use the derived dust properties and extend the radiative transfer computations to

170   *diurnal mean* and to DRE at surface. The rest of this paper is organized as follows: Section 2

171   describes the data and model used. Section 3 presents the sensitivity of dust DRE to dust size,

172   shape and refractive index. Section 4 discusses diurnally averaged net DRE of dust aerosols and

173   uncertainty analysis. Section 5 concludes the article.

174

175   **2. Data and Models**

176   **2.1 The CERES- CALIPSO-CloudSat -MODIS (CCCM) product**

177   To estimate instantaneous dust DRE, we use aerosol and radiation remote sensing products

178   from the A-Train satellite sensors, namely, the integrated CERES, CALIPSO, CloudSat, MODIS

179   merged product (CCCM) developed by [*Kato et al.,* 2011]. In the CCCM product, high-resolution

180   CALIOP, CloudSat and MODIS retrievals are collocated with 20-km CERES footprints. For each

181   CERES footprint, the CCCM product provides the TOA flux observations (both SW and LW)

182   from CERES, aerosol (MOD04 "Dark Target" product [*Remer et al.,* 2005]) and cloud (MOD06

183   [*Platnick et al.,* 2003]) properties retrieved from MODIS, aerosol optical thickness for each aerosol

184   layer from CALIOP [*Winker et al.,* 2010] and cloud vertical profile from the combination of

185   CALIOP and CloudSat [*Kato et al.,* 2010]. Up to 16 aerosol layers identified by CALIOP are kept

186   within a CERES footprint. *Figure 1* shows the JJA mean aerosol optical depth (AOD) from the

187 CALIOP observations reported in the CCCM product. Clearly, the transported dust aerosols lead

188 to enhanced AOD in the tropical North Atlantic region.

189 In addition to the "raw" retrievals, the CCCM product also provides post-processed flux

190 computations for each CERES pixel based on derived aerosol and/or cloud extinction profiles,

191 which is done in the following steps. First, the CALIOP aerosol retrievals within each CERES

192 pixel are averaged to obtain the aerosol extinction profile at the 0.5 µm reference wavelength.

193 Then, the aerosol type and associated spectral optical properties, e.g., extinction coefficient, single-

194 scattering albedo, and asymmetry factor are specified mostly based on the aerosol type simulations

195 from the Model of Atmospheric Transport and Chemistry (MATCH [*Collins et al.,* 2001], with

196 the exception of dust aerosols. If CALIOP observes dust aerosols (dust and polluted dust), the

197 aerosol type is set to dust. This is based on the consideration that the depolarization observation

198 capability of CALIOP is ideal for dust detection because the nonsphericity of dust can cause

199 significant depolarization in contrast to most other types of aerosols. Finally, the aerosol extinction

200 profiles and the aerosol spectral optical properties are used to compute the broadband fluxes at

201 both TOA and surface and for both SW and LW under 2 conditions: 1) with aerosol, 2) without

202 aerosol, so that the aerosol DRE can be derived from the difference of the two conditions.

203 Temperature and humidity profiles used in flux computations are from the Goddard Earth

204 Observing System (GEOS-5) Data Assimilation System reanalysis [*Rienecker et al.,* 2008].

205

206 **2.2 Dust Physical and Optical models**

207 To investigate the sensitivity of dust DRE to microphysical and optical properties of

208 particles, we use several sets of widely used or newly obtained dust size distribution, dust shape

209 distribution and dust refractive index.

210   Two dust particle size distributions (PSD) shown in *Figure 2*, are considered in this study.

211   One PSD is inferred based on AERONET ground-based retrievals at Cape Verde site (16°N, 22°W)

212   from [*Dubovik et al.,* 2002] (referred to as "AERONET" PSD). The other dust PSD is obtained

213   from the recent airborne measurements of transported Saharan dust from the Fennec 2011 field

214   campaign over both the Sahara (Mauritania and Mali) and the eastern Atlantic Ocean, between the

215   African coast and Fuerteventura. Ryder et al. [2013a] separate the PSD measurements from this

216   campaign into three broad categories: fresh, aged, SAL (acronym for "Saharan Air Layer"). The

217   fresh category over the Sahara represents dust uplifted no more than 12 hours prior to measurement;

218   the aged category over the Sahara represents dust aerosols mobilized 12 to 70 hours prior to

219   measurement; the SAL category represents dust aerosols transported over the adjacent east

220   Atlantic, mostly from flights over Fuerteventura, Canary Islands (28°N, 13°W). All these

221   categories come from the mean of vertical profile observations (excluding the marine boundary

222   layer for SAL categories). The Fennec airborne PSD dataset is particularly novel, in that larger

223   particle sizes were measured than has been done previously in dust layers, with the exception of

224   Weinzierl et al., 2011, and that errors due to sizing uncertainties have been specifically quantified

225   (see Ryder et al., 2013b and Ryder et al., 2015 for full details). Because this paper focuses on the

226   Tropical Atlantic Ocean region, we use dust size distribution in the SAL category (referred to as

227   the "Fennec-SAL PSD"). Evidently from *Figure 2*, the Fennec-SAL PSD, which peaks around

228   5~6 µm and has a significant fraction of particles with $r > 10$µm, is much coarser than the

229   AERONET PSD, which peaks around 1~2 µm and has almost no particles $r > 10$µm.

230   The dust refractive indices are taken from three sources:

231   (1) The Optical Properties for Aerosols and Clouds database (OPAC) [*Hess et al.,* 1998],

232   which has been widely used in climate models and satellite remote sensing algorithms.

233   (2) A merger of remote sensing based estimates of dust refractive indices in the shortwave

234   from 0.5 µm to 2.5 µm [*Colarco et al.,* 2014], drawn from Kim et al. [2011] in the visible, and

235   Colarco et al. [2002] in the UV and (referred to as "Colarco-SW"). Kim [2011] collected the

236   AERONET (V 2) retrievals from 14 sites over North Africa and the Arabian Peninsula. Then the

237   dust refractive index is derived from the dust dominant cases for these sites selected based on the

238   combination of large aerosol optical depth (AOD $\geq$ 0.4 at 440 nm) and small Ångström exponent

239   ($Å_{ext} \leq 0.2$) to select the dust cases. Colarco et al. [2002] derived the dust refractive index in the UV

240   by matching the simulated dust radiative signature in the UV with the satellite observations from

241   the Total Ozone Mapping Spectrometer.

242   (3) The refractive indices in the LW from 3µm ~15µm from Di Biagio et al. [2017]

243   (referred to as "Di-Biagio-LW"). This database is based on the laboratory measurements of 19

244   natural soil sample from 8 regions: northern Africa, the Sahel, eastern Africa and the Middle East,

245   eastern Asia, North and South America, southern Africa, and Australia. The refractive index from

246   the Mauritania site is selected for this study because it is geographically close to the Fennec field

247   campaign.

248   *Figure 3* compares the real and imaginary parts of the refractive index for each of these

249   data sets. In the SW, the imaginary part of the OPAC refractive index is much greater than that of

250   Colarco-SW, which implies that dust aerosols based on the OPAC refractive index is more

251   absorptive. In the LW, the Di-Biagio-LW refractive index is smaller than the OPAC values in

252   terms of both the real and imaginary parts.

253   Dust aerosols are generally nonspherical in shape. Spheroids have proven to be a

254   reasonable first-order approximation of the shape of nonspherical dust [*Dubovik et al.,* 2006,

255   *Mishchenko et al.,* 1997]. The shape of a spheroid particle is determined by the so-called aspect

256　ratio, i.e., ratio of the polar to equatorial lengths of the spheroid. In our study, two spheroidal shape

257　distributions are used for computing the optical properties of non-spherical dust: (1) a size-

258　independent aspect ratio distribution from Dubovik et al. [2006] (see Figure 4a) and (2) a size-

259　dependent aspect ratio distribution extracted from Table 2 in Koepke et al. [2015], which is

260　discretized from measurement data of Kandler et al. [2009] (Figure 4b). The Dubovik et al. [2006]

261　shape distribution employs both oblate (aspect ratio < 1) and prolate (aspect ratio > 1) spheroids,

262　while the Kandler et al. [2009] shape distribution considers only prolate spheroids. For comparison

263　purpose, we also include spherical dust in our sensitivity studies. We use the Lorenz-Mie theory

264　code of Wiscombe [1980] to compute the optical properties of spherical dust particles. The optical

265　properties of spheroidal dust particles are derived from the database of Meng et al. [2010] . Note

266　that we assume volume equivalent radius for the AERONET-PSD to be consistent with Dubovik

267　et al. [2006] and the maximum dimension for Fennec-SAL PSD to be consistent with Ryder et al.

268　[2013b].

269

270　**2.3 Radiative transfer modeling**

271　　　The Rapid Radiative Transfer Model (RRTM) [*Mlawer et al.,* 1997] is used to compute

272　both SW and LW radiative fluxes for both clear and dusty atmospheres. RRTM retains reasonable

273　accuracy in comparison with line-by-line results for single column calculations. It divides the solar

274　spectrum into 14 continuous bands ranging from 0.2 µm to 12.2 µm and the thermal infrared (3.08

275　µm -1000 µm) into 16 bands. We explicitly specify the spectral AOD, ω and g of dust aerosols

276　for every band in the radiative transfer simulations.

277　**3. Case Selection and Observation-based Estimate of Instantaneous Dust DRE**

278　**3.1 Selection of cloud-free and dust-dominant cases in the CCCM product**

279   In this study, we focus on the Saharan dust outflow region in North Atlantic marked by the

280   box in Figure 1 (10º N ~ 30º N, 45º W ~ 20º W). This selection is based on several considerations.

281   Firstly, during the summer months (JJA) this region is dominated by transported dust aerosols

282   from Sahara. Secondly, because the ocean surface is dark, dust aerosols have a strong negative

283   DRE_{sw} in this region. Thirdly, the abovementioned AERONET Cape Verde and Fennec-SAL PSD

284   measurements are made in the vicinity of this region. Finally, the dust DREs in this region have

285   been extensively studied in the literature, making it easier for us to compare our results with

286   previous work.

287   We first select cloud-free and dust-dominant CERES pixels in the region from four summer

288   seasons (2007~2010) of the available CCCM product. Within each CERES pixel, the CCCM

289   product report two cloud masks, one from CALIOP and the other from MODIS. The former is

290   more sensitive to optically thin clouds but has a very narrow spatial sampling rate available only

291   along the CALIOP ground track. The latter provides the cloud mask for the entire CERES pixel

292   but may miss thin clouds. Because of the relative large footprint size (~20 km), the cloud-free

293   condition actually poses a very strong constraint on the CERES product. Out of the total 36165 of

294   CERES pixels in this region from 4 seasons of data, we found 1663 (only 5%) of cloud-free pixels

295   according to the CALIOP cloud mask. The sampling is further reduced to 464 (only 1.3%) if the

296   MODIS cloud mask is used to ensure the entire CERES footprint is cloud-free. This result is not

297   surprising because the MODIS cloud mask is more "clear-sky conservative", i.e., it tends to label

298   a pixel as cloudy if there is any ambiguity in its cloud mask test [*Ackerman et al.,* 1998]. A

299   comparison of collocated CALIOP and MODIS cloud mask along the CALIOP track by [*Holz et*

300   *al.,* 2008] reveals that MODIS masks more pixels as clear-sky than CALIOP does in the tropical

301   Atlantic dust outflow region (see their Fig. 3a), which is consistent with our result.

302   After selecting the cloud-free cases, we use the aerosol type information in the CCCM

303   product to further select dust-dominant cases (i.e., more than 90% of the aerosols within a given

304   CERES pixel are attributed to dust, in terms of area coverage). As aforementioned, the CCCM

305   product relies on CALIOP observations for detecting dust aerosols. After imposing the dust-

306   dominant condition, we are left with a total of 607 and 245 cloud-free and dust-dominant CERES

307   pixels, if CALIPSO and MODIS cloud mask are used, respectively. Furthermore, we found that

308   within these selected pixels 153 out of 607 cases and 87 out of 245 cases have both CALIOP and

309   MODIS aerosol optical depth (AOD) retrievals in the CCCM product, and the rest (454 out of 607

310   cases and 158 out of 245 cases) have AOD retrievals only from the CALIOP, but no AOD retrieval

311   from MODIS. The reason for this is unclear and beyond the scope of this study, but perhaps due

312   to the more rigorous quality control used in the passive aerosol retrieval from MODIS [*Remer et*

313   *al.,* 2005].

314

315   **3.2 Observation-based estimate of instantaneous dust DRE**

316   Many previous studies have shown that the aerosol DRE_{SW} over the dark ocean surface is

317   approximately linear with the AOD. The increasing rate of the magnitude of DRE_{SW} with AOD is

318   called the DRE_{SW} efficiency which is an important and useful quantity in many applications such

319   as aerosol model evaluation [*Zhou et al.,* 2005]. We note that DRE_{SW} depends on solar zenith angle

320   (SZA). However, Because the selected region is relatively small, the SZA at the A-Train overpass

321   time in the domain only varies slightly among our selected cases, from 20° to 28°. Considering

322   the limited sample size and the small SZA variation, we therefore estimate DRE efficiency based

323   on the combination of all selected cases without breaking them into smaller SZA intervals.

324   Because of the nearly linear relationship between DRE_{SW} and AOD, the CERES TOA flux

observation and the collocated AOD retrievals from either CALIOP or MODIS can be combined to derive an observation-based estimate of the *instantaneous* dust DRE. *Figure 5* shows linear regressions of CERES measured upward SW flux at TOA with satellite retrieved AOD for the selected cloud-free and dust dominant cases. Black dots and lines are for selected cases using the CALIOP cloud mask. For the 153 cases with both CALIOP and MODIS AOD retrievals, the combination of CERES and MODIS (*Figure 5*a) leads to a DRE_{SW} efficiency of dust -49.7 ± 7.1 W/m²/AOD (AOD is at 0.5 µm) with a linear regression R^2 value of 0.69. The uncertainty, i.e., ± 7.1 W/m²/AOD, associated with the regression line coefficients is estimated based on the 1- σ (one standard deviation) errors following Hsu et al. [2000]. The combination of CERES flux and CALIOP AOD (*Figure 5*b) leads to a DRE_{SW} efficiency of -36.5 ± 4.8 W/m²/AOD based on 1- σ error with a R^2 value of 0.5. To investigate the impact of different cloud mask, we also show the regression results derived from the cases selected based on MODIS cloud mask in Figure 5 (red dots and lines). We notice that the results are very similar to those based on the CALIOP cloud mask. Therefore, we conclude that the selection of cloud mask has negligible impact on our estimation of DRE and the main uncertainty is associated with the AOD retrieval. Considering that the MODIS and CALIOP aerosol retrievals are based on completely different methods, some difference between the two are not surprising. The tighter correlation between MODIS AOD and TOA upward SW flux is expected because MODIS retrieval is based on the reflected spectral solar radiation, whereas the CALIOP AOD retrievals are based on the inversion of backward scattering lidar signals. The potential reasons for the differences between CALIOP and MODIS AOD retrievals are beyond the scope of this study. Interested readers are referred to a couple of recent comparison studies by Kim et al. [2013] and Ma et al. [2013].

347   In summary, the *instantaneous* dust DRE$_{SW}$ efficiency in the selected region during

348   summer season is –49.7 $\pm$7.1 W/m^2/AOD based on CERES-MODIS observations and –36.5 $\pm$4.8

349   W/m^2/AOD based on CERES-CALIOP observations. With the DRE$_{SW}$ efficiency the DRE$_{SW}$ can

350   be easily derived from the AOD observations. The *instantaneous* DRE$_{SW}$ estimated from the

351   CERES-MODIS and CERES-CALIOP data is –14.2 $\pm$ 2.0 W/m^2 and –10.4 $\pm$1.4 W/m^2,

352   respectively (see Table 1).

353   In addition to the SW flux measurement, the CCCM product also provides the CERES

354   measurement of LW flux at TOA. Figure 6 shows the histograms of the broadband outgoing

355   longwave radiation (OLR) measured by CERES for the selected cases. Note that besides dust AOD,

356   OLR also strongly depends on other factors such as surface temperature, atmospheric profiles and

357   dust altitude. As a result, there is a high variability in those abovementioned factors among the

358   selected 607 cases. Therefore, it is not possible to derive the DRE$_{LW}$ efficiency and DRE$_{LW}$ in the

359   same way as we did for the SW. Here we use a different method. To estimate the DRE$_{LW}$, we first

360   computed the dust-free OLR based on ancillary data of surface temperature and atmospheric

361   profiles reported in the CCCM which is from the GEOS Model of NASA's Global Modeling and

362   Assimilation Office (GMAO) [Kato et al. 2011]. Then, the DRE$_{LW}$ can be estimated from the

363   difference between CERES observed OLR (i.e., blue solid line in Figure 6) and the computed dust-

364   free OLR (i.e., black dashed line in Figure 6). We refer to this method as "*semi-observation based*"

365   as it is based on the combination of observed dust-laden OLR and computed dust-free OLR. To

366   test if our computed dust-free OLR has any potential bias due to, for example, errors in the

367   ancillary data (i.e., atmospheric gas and temperature), we selected 75 cloud free cases in the same

368   region and season with no dust detected by CALIPSO. Note that because of the small dust loading

369   in these cases the computed OLR at TOA mainly depends on the accuracy of ancillary data of

370 surface temperature and atmospheric profiles. Therefore, the comparison between the computed

371 OLR and CERES measurements of those cases can inform us if there is any potential bias in our

372 computation of dust-free OLR. It turns out that the difference between RRTM and CERES OLR

373 has a mean value around 0.7 W/m^2 with standard deviation around 3.8 W/m^2 (not shown).

374 Therefore, in the following analysis all our dust-free OLRs are reduced by 0.7 W/m^2 to account

375 for this positive bias, which leads to a semi-observation-based *instantaneous* DRE_{LW} of dust at

376 2.7 $\pm$ 0.32 W/m^2 with the 95% confidence level.

4. Sensitivity of Dust DRE to Microphysical and Optical Properties of

Particles

379   The cloud-free and dust-laden cases from the CCCM product facilitate an ideal testbed for

380 investigating the sensitivity of dust DREs to the microphysical (i.e., PSD and shape) and optical

381 (i.e., refractive index) properties of dust. We use the aerosol extinction profiles at the 0.5 µm from

382 the CCCM product (which is based on CALIOP/CALIPSO observations) and different

383 combinations of the dust properties to drive multiple sets of radiative transfer simulations of dust

384 DREs. Through comparisons of the radiative transfer simulations with CERES observation, we

385 study how the physical and optical properties influence both the DRE_{SW} and DRE_{LW} of dust. It

386 should be mentioned here that the CCCM product also use the same methodology to generate the

387 aforementioned post-processed flux profile. In the analysis, we will also compare our dust DRE

388 simulations with the results provided in the CCCM products.

4.1 Sensitivity to dust size and refractive index

390   In the first sensitivity study, we study the influences of dust size and refractive index on

391 the dust scattering properties and consequently dust DREs. Based on different combinations of the

392   PSDs (AERONET vs. Fennec-SAL) and SW refractive index (OPAC vs. Colarco-SW), we

393   simulate four sets dust spectral scattering properties (Figure 7), and correspondingly four sets of

394   dust DRE_{SW} efficiency (Figure 8). In the simulations, dust particles are assumed to be spheroidal

395   and the aspect ratio distribution from Dubovik et al. [2006] (see Figure 4a) is used. The OPAC-

396   LW refractive index is used. The impacts of dust shape distribution and LW refractive index on

397   dust DRE will be discussed later.

398   Figure 7 shows the scattering properties for the four different combinations of dust PSD

399   and refractive index. The extinction efficiency (Q_e) based on the Fennec-SAL PSD is significantly

400   larger than that based on the AERONET PSD (Figure 7a). The spectral shape is also different. The

401   Q_e based on the Fennec-SAL PSD is rather flat in the SW region due to its large size whereas the

402   Q_e based on the AERONET PSD decreases with wavelength. The Q_e shows no sensitivity to

403   refractive index in Figure 7a. It is because the Colarco-SW and OPAC-SW are different only in

404   the imaginary part (see *Figure 3*) which has minimal influence on Q_e. In contrast, the single

405   scattering albedo (SSA) in Figure 7b shows more sensitivity to refractive index. As expected, the

406   Fennec-SAL PSD and OPAC-SW combination (i.e., larger size and more absorptive refractive

407   index) has the smallest SW SSA while the AERONET PSD and Colarco-SW i.e., smaller size and

408   less absorptive refractive index) has the largest SW SSA. The other two combinations yield similar

409   SW SSA that are in between the abovementioned two extremes. The asymmetry factor (g) in

410   Figure 7c shows a primary sensitivity to size and a secondary sensitivity to refractive index.

411   Figure 7d shows spectral variation of dust AOD normalized with respect to AOD at 0.5µm.

412   The peak wavelength of solar radiation (0.5µm) and peak wavelength of terrestrial thermal

413   radiation (10µm) are highlighted with dashed lines. The 0.5 µm AOD is used as the reference for

414   normalization because as aforementioned, we use the 0.5 µm aerosol extinction profile in the

18

415 CCCM derived from CALIOP to drive our radiative transfer simulations. After spectral

416 normalization, one can see that given the same 0.5 µm AOD the 10 µm AOD based on the Fennec-

417 PSD is much larger than that based on the AERONET PSD by around 80%. This is an important

418 feature that has important implications for the DRE_{LW} of dust. The SW reflection of dust depend

419 not only on AOD, but also SSA and g. Figure 7e shows spectral variation of AOD*SSA*(1-g),

420 where AOD indicates dust load, is multiplied by SSA to take the scattered fraction, and then

421 multiplied by (1-g) to take the backscattered portion. It is a quantity more relevant for

422 understanding dust SW reflection. Evidently, this index suggests that the combination of smaller

423 size (AERONET PSD) and less absorptive refractive index (Colarco-SW) leads to most reflective

424 dust among the four sets of simulations, whereas the larger size (Fennec PSD) and more absorptive

425 refractive index (OPAC) combination generates least reflective dust. The other two combinations

426 are in between and somewhat similar.

427   Figure 8 shows the four sets of simulated TOA upward SW fluxes as a function of the input

428 AOD at 0.5 µm. For comparison purpose, the DRE_{SW} efficiency regression results based on

429 observations in *Figure 5*, as well as the results reported in the CCCM products, are also plotted.

430 Focusing on our computations first, we note that as expected the most reflective dust based on the

431 combination of AERONET PSD and Colarco-SW refractive index leads to the largest DRE_{SW}

432 efficiency (-70.5 W/m^2/AOD), while the least reflective dust based on the combination of Fennec-

433 SAL PSD and OPAC ref yields the smallest DRE_{SW} efficiency (-30.6 W/m^2/AOD). Clearly, these

434 results are outside of the range based on observations (i.e., $-36.5\pm4.8 \sim -49.7\pm7.1$ W/m^2/AOD),

435 suggesting they are too extreme. The other two combinations, i.e. AERONET PSD+OPAC-SW

436 and Fennec-SAL PSD + Colarco-SW, generate similar DRE_{SW} efficiency at -47.6 and -53.3

437 W/m^2/AOD, respectively, both comparable to the CERES-MODIS based value. Interestingly, the

438   DREsw efficiency based on the flux computations reported in the CCCM product is −81

439   W/m^2/AOD, even larger than that based on AERONET PSD + Colarco refractive index, suggesting

440   that the dust model used in the CCCM flux computations is too reflective in the SW. The

441   *instantaneous* DREsw and DREsw efficiency at surface for the two combinations that agree with

442   the CERES observation, i.e., AERONET PSD+OPAC-SW and Fennec-SAL PSD + Colarco-SW,

443   are given in the *Table 2*.

444   One additional point to note in Figure 8 is that, the TOA flux vs. AOD relations based on

445   the radiative transfer computations are much less scattered than those based on observations. The

446   R^2 value for the computation-based regressions all exceed 0.95, much higher than the observation-

447   based results in Figure 5. This is because, in reality the TOA flux is influenced not only by AOD,

448   but also many other factors, such as surface reflectance variation, boundary layer aerosols that

449   might not be undetected by satellite, uncertainty in satellite retrieval algorithm. Most of these

450   factors are not accounted for in the radiative transfer computations, leading to a near perfect

451   correlation between TOA flux and input AOD. This should not be interpreted as a lack of

452   variability, rather than a smaller uncertainty.

453   On one hand, the results in Figure 8 are encouraging, as they suggest that a relatively simple

454   combination of dust size and refractive index can enable us to simulate the dust DREsw that are

455   comparable with observations. On the other hand, the fact that two different dust models lead to

456   similar DREsw efficiency simulation, both comparable with observation, points to a long-lasting

457   problem in aerosol remote sensing. That is, different combinations of aerosol microphysical and

458   optical properties can lead to similar radiative signatures. The combination of smaller dust size

459   with more absorptive refractive index is as good as the combination of larger size with less

460   absorptive refractive index, as long as DREsw is concerned.

461   But are the two combinations also equal in terms of closing the LW radiation? This is an

462 important question, because ideally an appropriate dust model should close both SW and LW

463 radiation. To address this question, we extend our radiative transfer simulations to the LW. It is

464 important to point out that the LW and SW dust radiative properties are not independent but related

465 through the physical properties of dust. For example, the AOD at a given wavelength λ in LW is

466 related to the visible AOD through

$$AOD(\lambda) = AOD(0.5\mu m)\frac{Q_e(\lambda)}{Q_e(0.5\mu m)}, \tag{1}$$

467 where Q_e is the extinction efficiency that is determined by dust size, shape and refractive index.

468 The dust size and shape are obviously independent of wavelength and therefore connect the SW

469 and LW. Even the refractive index in the SW and LW regions should be physically self-consistent

470 because refractive index is determined by the chemical composition of dust. Unfortunately,

471 because the refractive index measurements are often made either for SW only or LW only, there

472 is a lack of measurement of dust refractive index measurement from visible all the way to thermal

473 infrared.

474   In our computations, we first use the LW dust refractive index from OPAC to compute the

475 dust LW scattering properties and the corresponding OLR. Based on the same OPAC-LW

476 refractive index, the Fennec-SAL PSD yields an instantaneous DRE$_{LW}$ of +3.0 W/m^2 at TOA and

477 +7.7 W/m^2 at surface (see *Table 3*). The results based on the AERONET PSD are significantly

478 smaller, +1.8 W/m^2 at TOA and +4.7 W/m^2 at surface. This difference between the two PSDs can

479 be easily understood with Figure 7b. Given the same visible AOD, the coarser Fennec PSD has a

480 larger infrared AOD than the AERONET PSD, and therefore stronger warming effects in the LW.

481   The more important question is which one, Fennec or AERONET PSD, leads to OLR

482 simulations that agree better with the CERES observation? The differences between the computed

483 OLRs and the CERES measurements of OLR for the selected dust cases are shown in *Table 4*,

484 together with the significance test results, i.e., 't-score' and 'p-value' from the Student's t-test.

485 Interestingly, the OLRs based on the combination of AERONET PSD + OPAC-LW refractive

486 index are systematically warmer (larger) than CERES measurements by an average of 0.9 W/m^2.

487 The high t-score of 2.36 and low p-value of 0.02 indicate this warm bias to be statistically

488 significant. In contrast, the OLRs based on the combination of Fennec PSD + OPAC-LW refractive

489 index have a bias only at –0.5 W/m^2 and a p-value (0.55) significantly larger than the commonly

490 used 0.05 threshold, which means that OLR of this dust model is statistically indistinguishable

491 from the CERES measurements. Then, to investigate the sensitivity of the computation to LW dust

492 refractive index, we performed the computations again based on the Di Biagio et al. LW refractive

493 index. As shown in *Table 4*, the OLR based on Fennec PSD is still better than that based on the

494 AERONET PSD, even though both sets deteriorate slightly in comparison with the results based

495 on the OPAC LW refractive index. Overall, the size difference is the primary reason for the fact

496 that the OLR based on Fennec PSD is systematically smaller than that based on the AERONET

497 PSD. As shown in Figure 7, due to size difference, the Q_e based on the Fennec-SAL PSD (coarser)

498 decreases at a slower rate than that based on the AERONET PSD (finer). As a result, according to

499 Eq. (1) given the same SW AOD, the Fennec-SAL has a larger LW AOD and therefore less OLR

500 than the AERONET PSD. In comparison with our results, the OLRs reported in the CCCM product

501 (not shown here) are on average 3.1 W/m^2 larger than CERES measurements. This warm OLR

502 bias of CCCM product in the LW is consistent with its "too reflective" bias in the SW in Figure 8.

503   The LW result in *Table 4* is interesting and important. First of all, it suggests that the LW

504 spectral region provides useful information content on dust properties that is complementary to

505 SW. As we see from Figure 8, the Fennec-SAL PSD + Colarco-SW refractive index and

506   AERONET PSD + OPAC-SW SW refractive combinations yield very similar SW radiation

507   simulations. However, only Fennec PSD can lead to reasonable LW radiation simulation. Secondly,

508   although the main point here is more about the usefulness of the information content in LW, the

509   fact that the coarser Fennec PSD leads to better OLR simulation than AERONET PSD and CCCM

510   product (based on MATCH) aligns with the recent studies (e.g., Kok et al. [2017]) arguing that

511   dust size tends to be underestimated in the aerosol simulation models.

512   Finally, as expected, the combination of Fennec PSD + OPAC-LW also yields the best

513   simulation of the dust DRE_{LW}, at 3.0 W/m^2, in comparison with the result derived from the CERES

514   OLR observations and RRTM dust-free OLR computation with ancillary data provided by CCCM

515   product (i.e., +3.4$\pm$0.32 W/m^2 based on CERES-CALIPSO combination).

516

517   **4.2 Sensitivity to dust shape**

518   In this section, we investigate the sensitivity of dust DRE to the shape (or shape distribution)

519   of dust. For all the computations in the last section, we have used the spheroidal dust model with

520   the aspect ratio distribution from Dubovik et al. [2006] (See Figure 4a). Now, we replace this

521   model with another spheroidal dust model by Kandler et al. [2009] shown in Figure 4b. For

522   comparison purpose, we also carry out another set of computation assuming spherical dust. For

523   dust size and refractive index, we use the Fennec-SAL and Colarco-SW/OPAC-LW refractive

524   index since dust DREs based on this combination has shown the best agreement with the

525   observations.

526   In Figure 9, we compare the scattering properties of dust based on three different shape

527   models. Overall, the two spheroidal models are very similar and both significantly different from

528   the spherical model. More specifically, in the SW the Q_e based on spheroidal models is

529   significantly larger than that based on spherical dust model. In the LW it is the opposite. The ω

530   in Figure 9b suggest that the spherical dust is more absorptive than spheroidal dust in the SW

531   region, when other things are equal. Figure 9d and e show the normalized the AOD with respect

532   to AOD(0.5 μm) and the spectral variation of the scattering index AOD*SSA*(1-g). From Figure

533   9d we can see that given the same SW AOD, the spherical model has the larger LW AOD than the

534   two spheroidal models. The comparison in Figure 9e reveals that the spherical dust model is less

535   reflective than the spheroidal model in the SW.

536   Figure 10 shows the radiative transfer simulations for the selected cases based on the three

537   dust shape models. The DRE$_{SW}$ efficiency based on the Kandler et al. [2009] is -48.3 W/m^2/AOD,

538   which almost identical to the -47.6 W/m^2/AOD based on the Dubovik et al. [2006] model. In

539   contrast, the DRE$_{SW}$ efficiency based on the spherical dust model is much smaller -39.8

540   W/m^2/AOD, which can be expected from the results in Figure 9e (i.e., spherical dust is less

541   reflective). Because the DRE$_{SW}$ efficiencies based on all three shape models are within the

542   observation-based values, we cannot tell if the spherical dust model is better or worse than the

543   spheroidal models.

544   As mentioned above, the two spheroidal dust models yield very similar OLR simulations

545   and are both statistically indistinguishable from the CERES observations. In contrast, the OLR

546   simulations based on the spheroidal dust models has a statistically significant -0.8 W/m^2 cold bias,

547   with a p-value of 0.03 (See Table 4). Overall, the r esults in Figure 10 and Table 4 indicate that

548   the two spheroidal models provide a slightly better, especially in LW, agreement with the

549   observations. Note that different shape models may have different angular and/or spectral signature

550   in terms of radiance, which is more important for satellite remote sensing. But this is beyond the

551   scope of this study and will be investigated in future work.

5. Diurnally Mean Dust DRE in North Atlantic

The DRE computations in the last section (i.e., Table 1~ Table 3) are *instantaneous* values corresponding to the overpassing time of Aqua around 1:30PM local time. The strong solar insolation makes the instantaneous DRE_{SW} much larger than DRE_{LW} in terms of magnitude, leading to a strong negative DRE_{net} (cooling) of dust. However, the DRE_{SW} operates only during daytime, while the DRE_{LW} operates both day and night. In addition, because of the availability of satellite observations only at TOA, we have focused only on the DRE at TOA in the analyses above. To appreciate the relative magnitude of DRE_{LW} with respect to DRE_{SW} we extend our DRE simulations and analysis from *instantaneous* to *diurnal mean,* and also from TOA to surface. Over tropical ocean, the OLR is most sensitive to sea surface temperature (SST). Our sensitivity study based on the 3-hour MERRA (Modern-Era Retrospective analysis for Research and Applications) data suggests that the diurnal SST variation in the tropical North Atlantic region is so small that the diurnal mean OLR is close to the *instantaneous* value. Similarly, we also found that the diurnal variation of atmospheric profile (e.g., water vapor) has negligible impact on the diurnal DRE_{SW} computation. Therefore, we only compute the diurnal variation of DRE_{SW} due to the change of solar zenith angle and ignore the small diurnal variation of DRE_{LW} as well as the impacts of atmospheric profile change on DRE_{SW}.

Table 5 summarizes the key results of the diurnal mean DRE_{SW} and DRE_{SW} efficiency at TOA, as well as at surface. In the SW, the two most reasonable combinations of PSD and refractive index, Fennec-SAL PSD + Colarco-SW and AERONET-PSD + OPAC-SW leads to similar TOA DRE_{SW} efficiency around -29 W/m^2/AOD, which is at the center of the $-16 \sim -41$ W/m^2/AOD range reported in Yu et al. [2006]. At the surface, the DRE_{SW} efficiency based on these two combinations are around -83 W/m^2/AOD, which is significantly stronger than the $-27 \sim -68$ W/m^2/AOD range reported in Yu et al. [2006]. It should be noted that we have limited this study

576 to dust-dominant cases, whereas the values in Yu et al. [2006] are based on simple domain average

577 and include other types of aerosol.

578   By combining the information in Table *3* and *Table 5*, we can easily derive the net DRE_{net}

579 of dust in the North Atlantic during summer. The TOA DRE_{net} based on the combination of

580 Fennec-SAL PSD + Colarco-SW + OPAC-LW refractive indices gives a regional mean DRE_{net} of

581 -6.9 W/m^2 and -18.3 W/m^2 at TOA and surface, respectively. In comparison, the corresponding

582 values based on the combination of AERONET PSD + OPAC-SW + OPAC-LW refractive indices

583 are -8.5 W/m^2 and -22.5 W/m^2, respectively. It is interesting and important to point out that the

584 DRE_{LW} is significant, about 17% ~ 36% (depending on the choice of PSD and refractive index) in

585 terms of magnitude with respect to the DRE_{SW}, and therefore not negligible in the DRE_{net}

586 regardless whether for TOA or surface.

587 **6. Summary and Discussions**

588   In this study, we use A-Train satellite observations reported in the CCCM product and

589 recent in situ measurements of dust properties to investigate the DREs of the dust aerosols in the

590 North Atlantic African dust outflow region during summer months. First, we select about 600

591 cloud-free and dust-dominant CERES pixels from 5 seasons of CCCM product. Based on these

592 cases, we first derive a set of observation-based instantaneous (corresponding to Aqua overpassing

593 time) DRE_{SW} efficiency and DRE_{SW} using the combination of CERES-measured TOA flux and

594 MODIS or CALIPSO retrieved dust AOD. The DRE_{SW} efficiency and DRE_{SW} based on CERES-

595 MODIS observation are -49.7 ± 7.1 W/m^2/AOD and -14.2 ± 2 W/m^2, respectively. The values

596 based on the CERES-CALIOP combination are -36.5 ± 4.8 W/m^2/AOD and -10.4 ± 1.4 W/m^2,

597 respectively. Using the combination of CERES-measured OLR (i.e., with dust) and computed

598 dust-free OLR based on ancillary data, we also derive a set of semi-observation-based TOA

599 DRE_{LW} between 2.38 ~ 3.72 W/m^2.

600   In the follow-up sensitivity study, we use the RRTM radiative transfer model to compute

601 the DRE of dust using the observed 0.5µm dust extinction profiles from CALIPSO under various

602 different assumptions of dust PSD, refractive index and shape distributions. We find that two dust

603 models, one based on Fennec-SAL PSD and Colarco-SW refractive index and the other on

604 AERONET PSD and OPAC-SW refractive index, provide the best fit to the observation-based

605 DRE_{SW} efficiency and DRE_{SW}. However, only the one based on the Fennec-SAL PSD, which is

606 much coarser than the AERONET-PSD, can also provide reasonable fit to the observation-based

607 DRE_{LW}. We also find that the DREs based on the two spheroidal dust models are quite similar to

608 each other, but more different from those based on spherical dust, suggesting that the detailed

609 shape distribution is less important in the calculation of dust DRE. Based on the dust model that

610 provides the best fit to the observation-based DRE, we estimate the diurnal mean dust DRE_{SW}

611 efficiency in the North Atlantic region during summer months (JJA) from 2007 to 2010 to be

612 around −28 and −82 $W/m^2/AOD$ at TOA and surface, respectively. The corresponding DRE_{SW} is

613 −9.9 W/m^2 and −26 W/m^2 at TOA and surface, respectively. The diurnal mean DRE_{LW} is about 3

614 W/m^2 at TOA and 7.7 W/m^2 at surface. As dust aerosol properties varies temporally and spatially,

615 DREs of dust aerosols also have high spatio-temporal variation. Therefore, it is worthy to extend

616 the analysis to other regions and years in future studies.

617   Our estimation of the instantaneous TOA DRE_{SW} efficiency is in reasonable agreement

618 with the values reported in a recent study by Mishra et al. [2017]. Their observations are from a

619 satellite instrument similar to CERES, called Megha-Tropiques-ScaRaB (MT- ScaRaB). Flying in

620 a low-inclination orbit, this instrument is able to observe the TOA radiation in the tropical region

621 at various local times. Using 4 years MT- ScaRaB radiation and MODIS AOD observation, Mishra

622 et al. [2017] estimate that the instantaneous TOA DRE_{SW} corresponding to a solar zenith angle of

623 ~40° in the North Atlantic region is about −40 $\pm$ 3 W/m^2/AOD, which is in between our range of

624 −49.7$\pm$7.1 W/m^2/AOD and −36.5$\pm$4.8 W/m^2/AOD. Our estimation of the diurnal mean TOA

625 DRE_{SW} efficiency (−28 W/m^2/AOD) is in between the −18 W/m^2/AOD reported in Mishra et al.

626 [2017] and −35 W/m^2/AOD reported in Li et al. [2004]. The difference may result from different

627 selection of cases and domain. Note that our analysis is limited to cloud-free and dust-dominant

628 cases that are selected based on MODIS and CALIOP observations.

629   Due to the lack of study on dust DRE_{LW} in this region, it is difficult to find a comparable

630 result the literature to validate our estimate of DRE_{LW}. Nevertheless, our result that the positive

631 DRE_{LW} cancels about 30% of the negative DRE_{SW} in the computation of the diurnal mean net dust

632 DRE is in agreement with many previous studies attesting the importance of dust DRE_{LW} (e.g.,

633 Zhang et al. 2003, Haywood et al. 2005). Note that over land, e.g., the Sahara Desert, the brighter

634 surface reflectance will reduce the cooling effect of DRE_{SW} or even leads to warming (positive)

635 DRE_{SW}. At the same time, the hot surface temperature during daytime may result in DRE_{LW}

636 significantly larger than that over ocean. Therefore, the DRE_{LW} is expected to be even more

637 significant in comparison with DRE_{SW}, over land than over ocean, which is an interesting topic for

638 future studies.

639   Another interesting result from this study is that given the same visible AOD dust particle

640 size and dust absorption in the SW can compromise each other in determining dust DRE_{SW}. As a

641 result, it is difficult to specify both variables using the SW radiation alone. In such case, the LW

642 radiation could provide complementary and important information on dust properties, especially

643 dust particle size. Most of the current aerosol property retrieval algorithms use only SW radiation

644 observations. There are also a few algorithms to retrieve dust properties using only LW radiation

645 observation [e.g., Pierangelo et al., 2004, DeSouza-Machado et al. 2006, Peyridieu et al., 2010].

646 It is worth exploring in future studies the possibility and benefit of retrieving dust properties

647 utilizing both the SW and LW observations.

648 Finally, as discussed in Section 3.1, because the selected region is quite cloudy, and the

649 footprint of CERES is relatively large, the sampling rate of cloud-free and dust dominant cases is

650 very low. An important question arises from the low sampling is whether our results are

651 representative. More specifically, one may wonder if our cloud-free cases are also representative

652 of the clear-sky part of those cloudy CERES pixels. To address this question, we investigated if

653 the dust properties (e.g., AOD and dust temperature) and meteorological conditions (e.g., surface

654 temperature and precipitable water) have any correlation with the cloud fraction. If the statistics

655 of the dust properties and meteorological conditions from our clear-sky cases are similar to those

656 from the cloudy cases, then our results are arguably representative of not only the clear-sky dust-

657 dominant CERES pixels, but also the clear-sky part of cloudy dust dominant CERES pixels. To

658 this end, we first check the AOD. This time we selected all the dust-dominant cases based on

659 CALIOP observations regardless of the cloud fraction. Then, we divided all the cases into 5 groups

660 according to the cloud fraction within the CERES pixel, i.e., 0~20%; 20~40% 40~60% 60~80%

661 and >80%. As shown in Figure 11a, the dust AOD from the cloudy groups is statistically larger

662 than that from our cloud-free cases, which also means larger DRE_{SW} if the DRE efficiency remains

663 the same. We don't know whether other dust properties, such as size, shape and refractive index,

664 are correlated with cloud fraction. Investigating this is extremely challenging, if not impossible,

665 using satellite observations. We have to leave this for future studies using other types of

666 measurements (e.g., in situ). In addition to dust AOD, we also checked the surface temperature,

667   the dust layer temperature (weighted by the dust extinction coefficient from CALIOP) and the total

668   amount of water vapor in the column. These quantities are potentially important for the DRE_{LW}.

669   As shown in the Figure 11, in terms of the surface temperature (Figure 11 b) and dust layer

670   temperature (Figure 11 c), the cloudy dust-dominant cases are almost identical to our cloud-free

671   dust-dominant cases. However, not surprisingly, we found that the cloud-free cases are drier than

672   the cloudy cases (Figure 11 c). Note that, given the same dust properties, an increasing of water

673   vapor increases the atmospheric opacity in the LW, which tends to reduce the dust DRE_{LW}. In

674   summary, if the dust particles properties (i.e., dust size, shape and refractive index) remain the

675   same, then the DRE_{SW} of dust in the clear-sky part of cloudy CERES pixels would be slightly

676   larger than that based on our results because of the larger AOD. In the LW, the larger AOD of the

677   clear-sky part of cloudy CERES pixels would lead to a larger DRE_{LW}, but on the other hand, the

678   increased humidity under cloudy conditions counteract the effect of larger AOD. The net result is

679   dependent on the relative importance of these two competing factors.

680

681

Figures and Tables:

682

683

684

685 Table 1 Observation-based instantaneous (at A-Train overpassing time) DRE and DREsw
686 Efficiency at the top of atmosphere (TOA). The values in the parenthesis for DRELW are based
687 on the assumption of 0.7 W/m² bias in our clear-sky OLR computation. See text for detail.

688

	TOA DRE_{SW} Efficiency $[W \cdot m^{-2} \cdot AOD^{-1}]$	TOA DRE_{SW} $[W \cdot m^{-2}]$	TOA DRE_{LW} $[W \cdot m^{-2}]$
CERES-MODIS AOD	-49.7±7.1	-14.2±2.0	3.1±0.60 (2.4±0.60)
CERES-CALIPSO AOD	-36.5±4.8	-10.4±1.4	3.4±0.32 (2.7±0.32)

689

690

691
692
693
694
695
696
697
698
699
700
701
702
703
704
705
706
707
708
709
710
711
712
713
714
715

716

717

718

719 Table 2 Instantaneous DRE$_{SW}$ and DRE$_{SW}$ Efficiency at TOA and Surface based on different
720 dust models (e.g., PSD, refractive index, and shape).

PSD	Refractive Index	Shape	TOA DRE$_{SW}$ efficiency (W/m²/AOD$_{0.5\mu m}$)	TOA DRE$_{SW}$ (W/m²)	Surface DRE$_{SW}$ efficiency (W/m²/AOD$_{0.5\mu m}$)	Surface DRE$_{SW}$ (W/m²)
Fennec-SAL	Colarco-SW	Dubovik	-47.6	-13.5	-179.4	-51.5
AERONET	OPAC-SW	Dubovik	-53.3	-15.5	-190.1	-55.0
Fennec-SAL	Colarco-SW	Sphere	-39.8	-11.4	-200.4	-58.2

721

722

723

724

725 Table 3 Instantaneous DRE$_{LW}$ based on different dust models. Note that the diurnal mean values
726 are almost identical to the instantaneous results due to small diurnal variation in the LW.

PSD	Refractive Index	Shape	TOA DRE$_{LW}$ efficiency (W/m^2/AOD$_{0.5\mu m}$)	TOA DRE$_{LW}$ (W/m^2)	Surface DRE$_{LW}$ efficiency (W/m^2/AOD$_{0.5\mu m}$)	Surface DRE$_{LW}$ (W/m^2)
Fennec-SAL	OPAC-LW	Dubovik	10.5	3.0	26.9	7.7
AERONET	OPAC-LW	Dubovik	6.3	1.8	16.4	4.7
Fennec-SAL	Di-Biagio-LW	Dubovik	8.4	2.4	18.9	5.4
Fennec-SAL	OPAC-LW	Sphere	12.6	3.6	32.9	9.4

727
728
729

730
731 Table 4 The difference in OLR between our computations and the CERES measurements for the
732 selected dust cases. The values in the table are based on the assumption of 0.7 W/m^2 bias in our
733 clear-sky OLR computation.

PSD	Refractive Index	Shape	Mean Difference	Standard Deviation	T-score	P-value
Fennec-SAL	OPAC-LW	Dubovik	-0.2	3.8	-0.62	0.55
Fennec-SAL	Di-Biagio-LW	Dubovik	0.3	3.7	0.83	0.41
Fennec-SAL	OPAC-LW	Kandler	-0.4	3.9	-0.9	0.54
Fennec-SAL	OPAC-LW	Sphere	-0.8	4.0	-2.1	0.033
AERONET	OPAC-LW	Dubovik	0.9	3.7	2.36	0.02
AERONET	Di-Biagio-LW	Dubovik	1.5	3.7	3.94	8.5e-5

734
735
736

737

738　Table 5 Diurnally mean DRE_{SW} and DRE_{SW} Efficiency at TOA and Surface

PSD	Refractive index	Shape	TOA DRE_{SW} Efficiency (W/m²/AOD)	TOA DRE_{SW} (W/m²)	Surface DRE_{SW} Efficiency (W/m²/AOD)	Surface DRE_{SW} (W/m²)
Fennec-SAL	Colarco-SW	Dubovik	-28	-9.9	-82.1	-26.0
AERONET	OPAC-SW	Dubovik	-29.4	-10.3	-85.7	-27.2
Fennec-SAL	Colarco-SW	Spherical	-22.8	-8.2	-89.6	-28.5

739
740

741
742
743
744
745
746
747
748
749
750
751
752
753
754
755
756
757
758
759
760
761
762
763
764
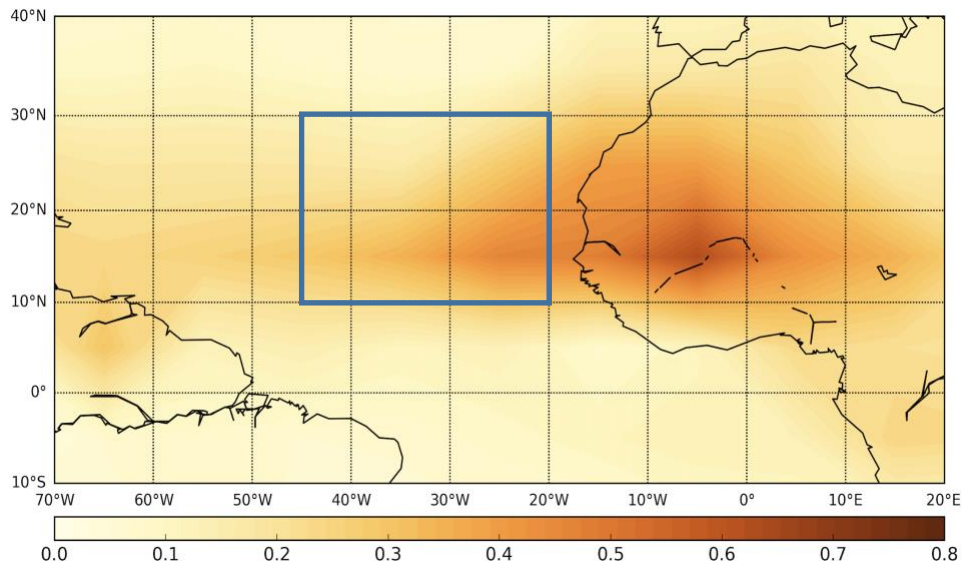
765
766 Figure 1 CALIPSO derived seasonal mean (JJA) dust aerosol optical depth (AOD) at 0.5 µm
767 averaged over five summers (2007~2010) in cloud free sky condition from the integrated
768 CALIPSO, CloudSat, CERES, MODIS merged product (CCCM).

769
770

771
772
773
774
775
776
777
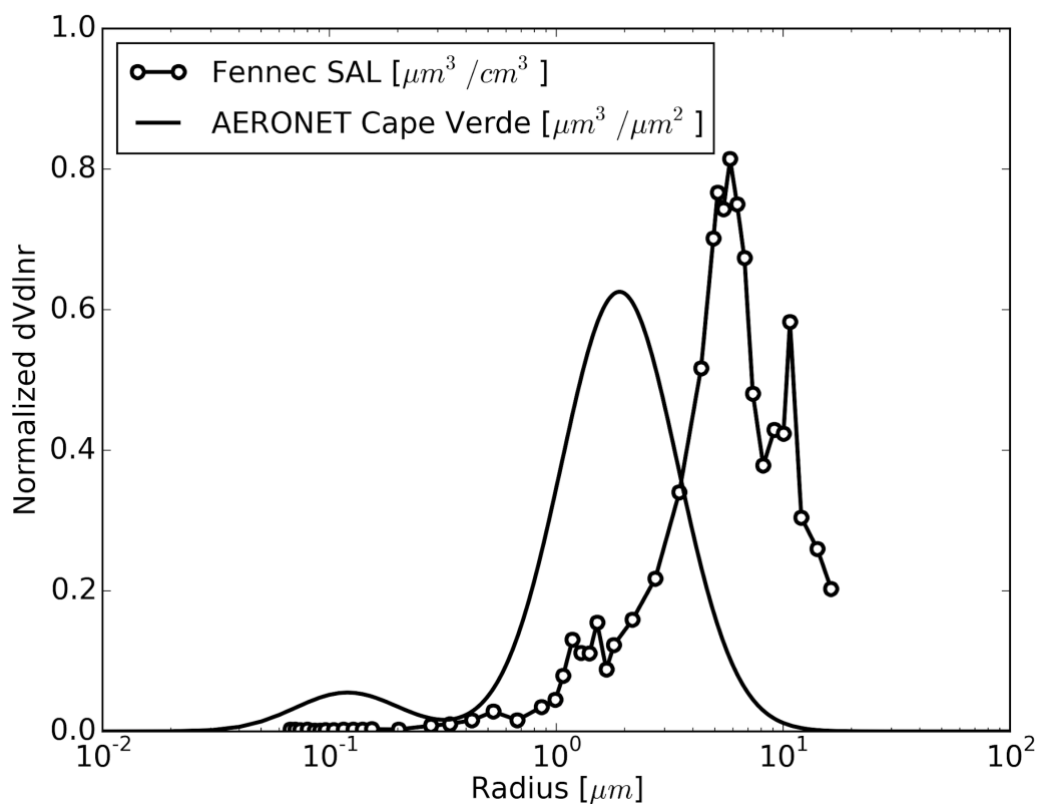
Figure 2 Size distributions of mineral dust used in this study. Fennec-SAL curve is from a new in-situ measurement of Saharan dust taken during the Fennec 2011 aircraft campaign [Ryder et al. 2013]. The solid curve represents desert dust size distribution retrieved from AERONET observations at Cape Verde site reported in Dubovik et al. [2002].

783
784

785
786
787
788
789
790
791
792
793
794
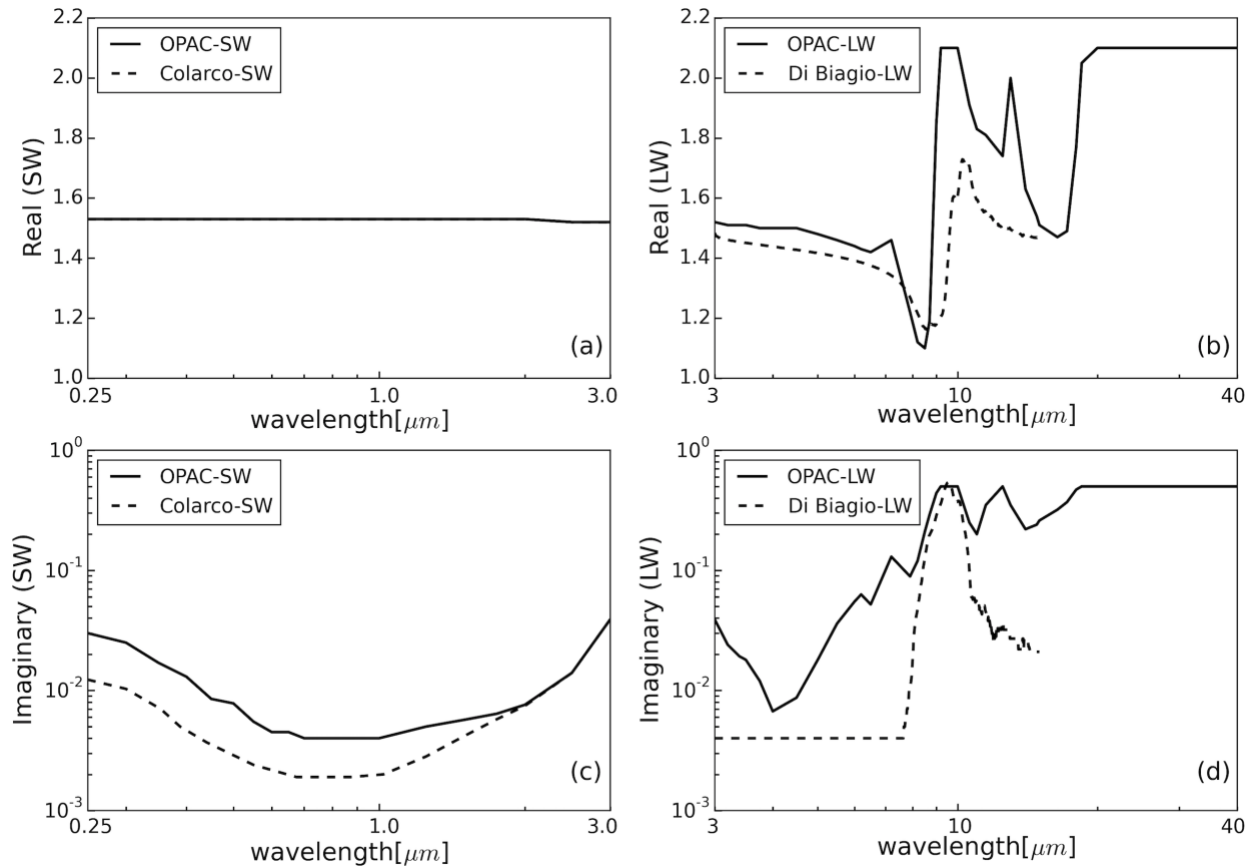
795
796 Figure 3 a) real and b) imaginary part of the SW dust refractive index from OPAC [Hess et al.
797 1998] and Colarco et al. [2014]; c) real and d) imaginary part of the LW dust refractive index
798 from OPAC [Hess et al. 1998] and Di Biagio et al. [2017].

799
800
801
802
803
804
805
806
807

808
809
810
811
812
813
814
815
816
817
818
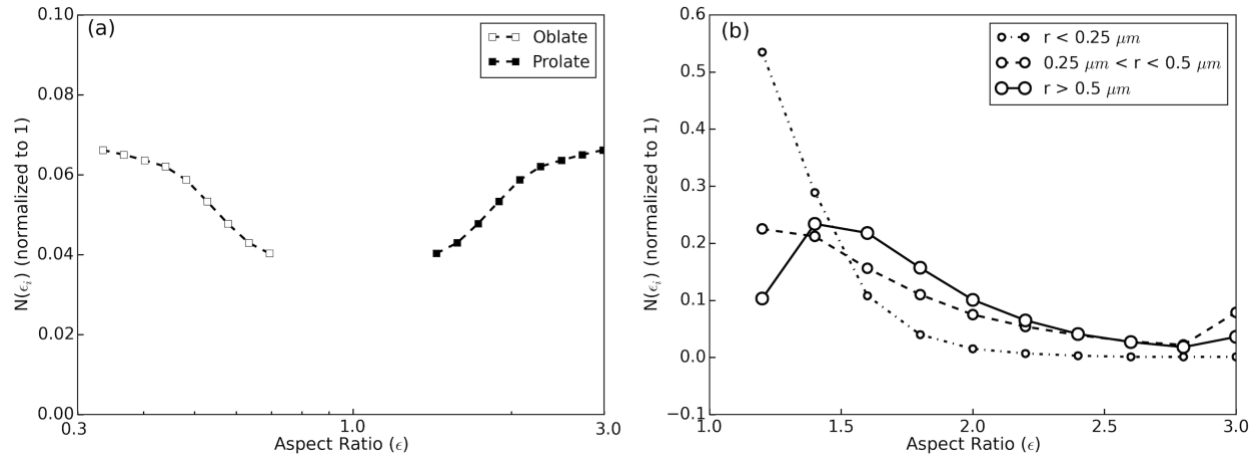
819
Figure 4 Two spheroidal dust shape distributions models a) shows aspect ratio distributions from Dubovik et al. [2006]. The lnε-interval is 0.09. b) shows aspect ratio distributions as function of particle radius interval discretized from measurement of Kandler et al. (2009). The first point of each line covers the measurement data from ε=1.0 to 1.3, the last point of each line covers ε > 2.9 and the other points cover ε-intervals of 0.2 Koepke et al. [2015].

825
826
827

828
829
830
831
832
833
834
835
836
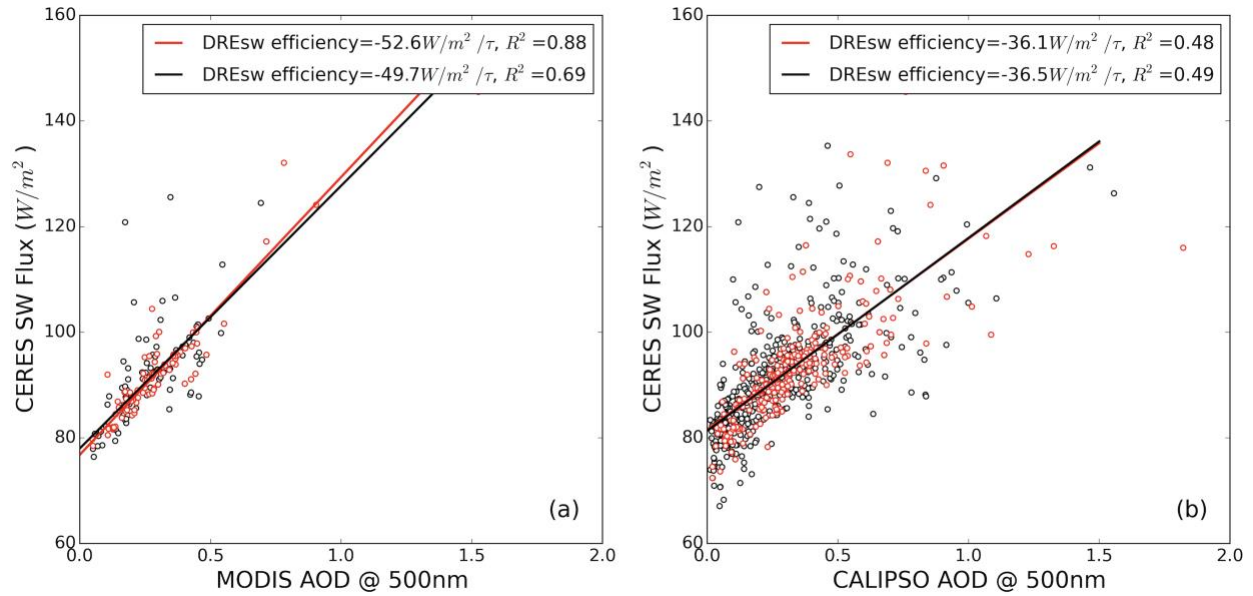
837
838
Figure 5 Linear regressions of CERES measured upward SW flux at TOA with satellite retrieved
AOD for the selected cloud-free and dust dominant cases (Black points represent the cases selected
using CALIPSO cloud mask along the ground track, red points represent the cases selected using
MODIS cloud mask over the entire CERES footprint). a) shows the regression results based on
MODIS AOD for cases (153 black points and 87 red points) with MODIS AOD retrievals. b) is
for all cases (607 black points and 245 red points) with CALIPSO AOD retrievals.

845

846
847
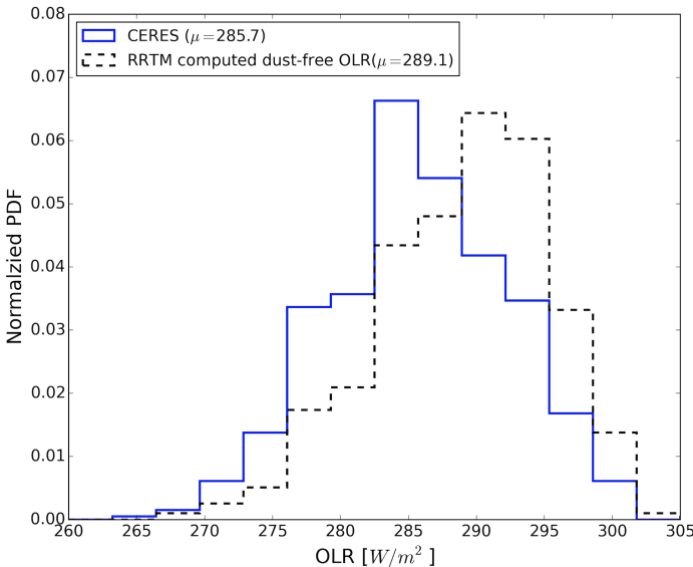
848
849   Figure 6 PDF of observed OLR from CERES (i.e., with dust) and computed dust-free OLR based
850   on the atmospheric profiles and surface temperature reported in CCCM.
851

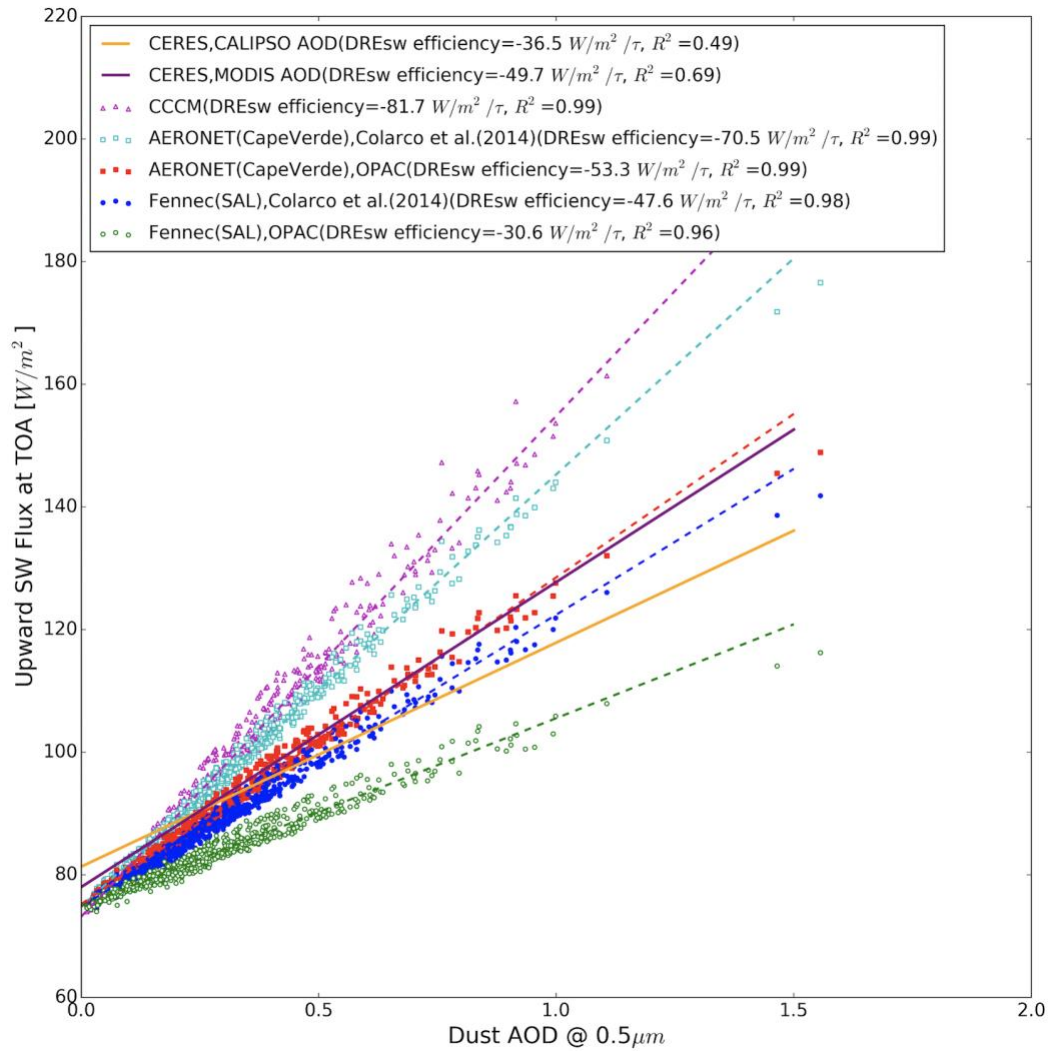852
853

854
855
856
857
858
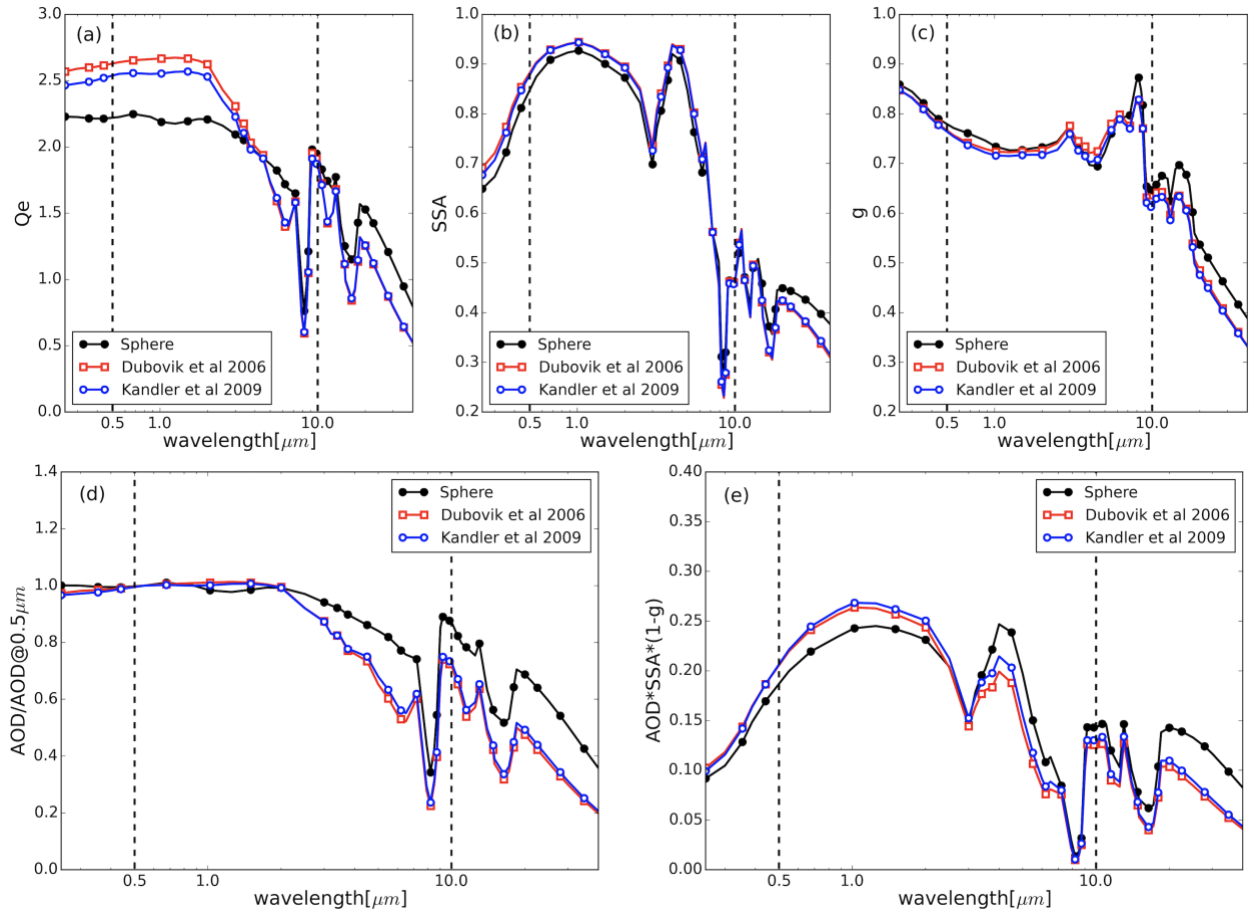859
860
861
862

863

864
865
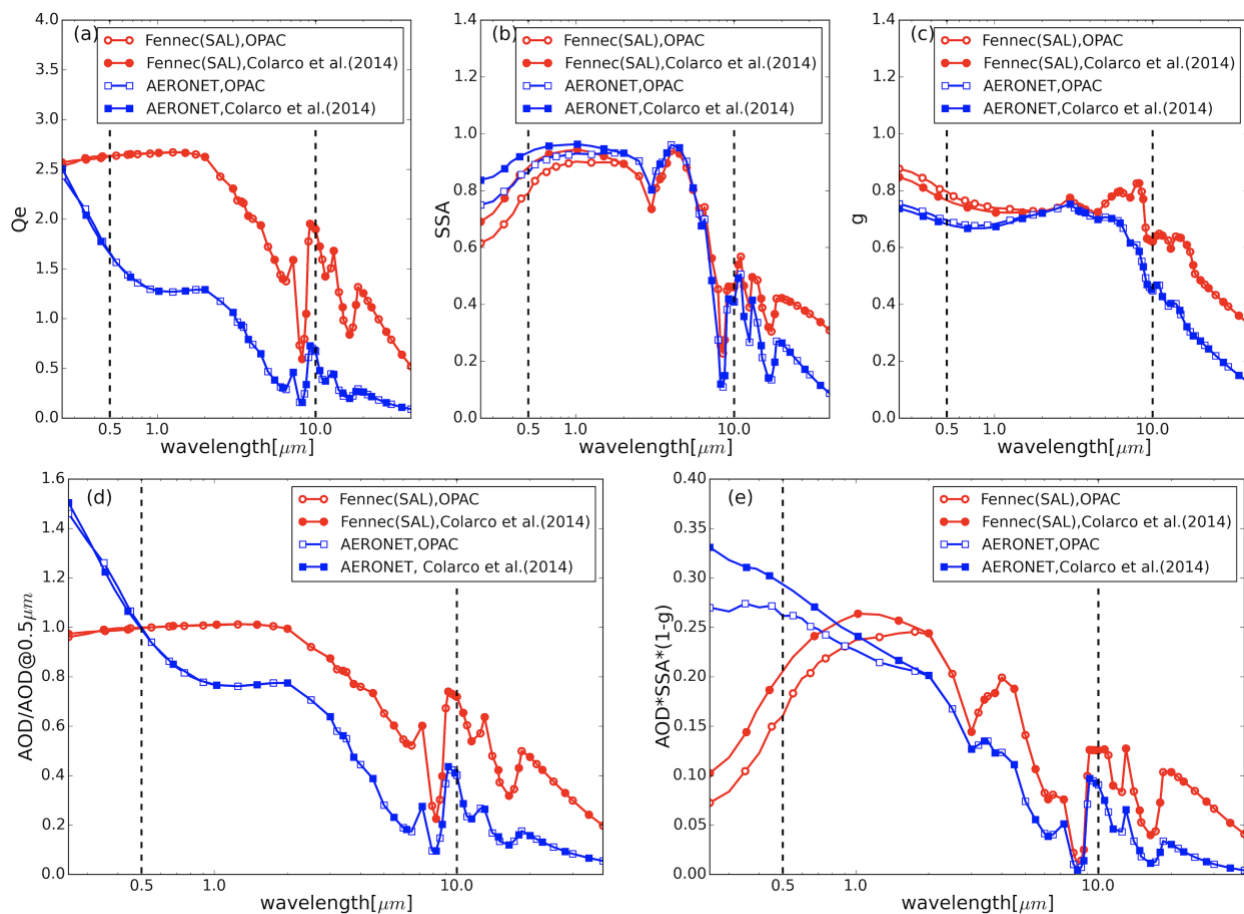
Figure 7 a) Extinction efficiency (Qe), b) single scattering albedo (SSA), c) asymmetry factor (g) d) normalized AOD with respect to AOD @ 0.5 µm, and e) AOD*SSA*(1-g) of dust aerosols based on different combination of PSD and refractive index. PSD type and refractive index type are indicated in legends.

870
871

872
873

874
875 Figure 8 The four sets of simulated TOA upward SW fluxes as a function of the input AOD at 0.5
876 µm. For comparison purpose, the DRE$_{sw}$ efficiency regression results based on observations in
877 Figure 5, as well as the results reported in the CCCM products, are also plotted.

878
879
880
881
882
883
884
885
886
887
888
889
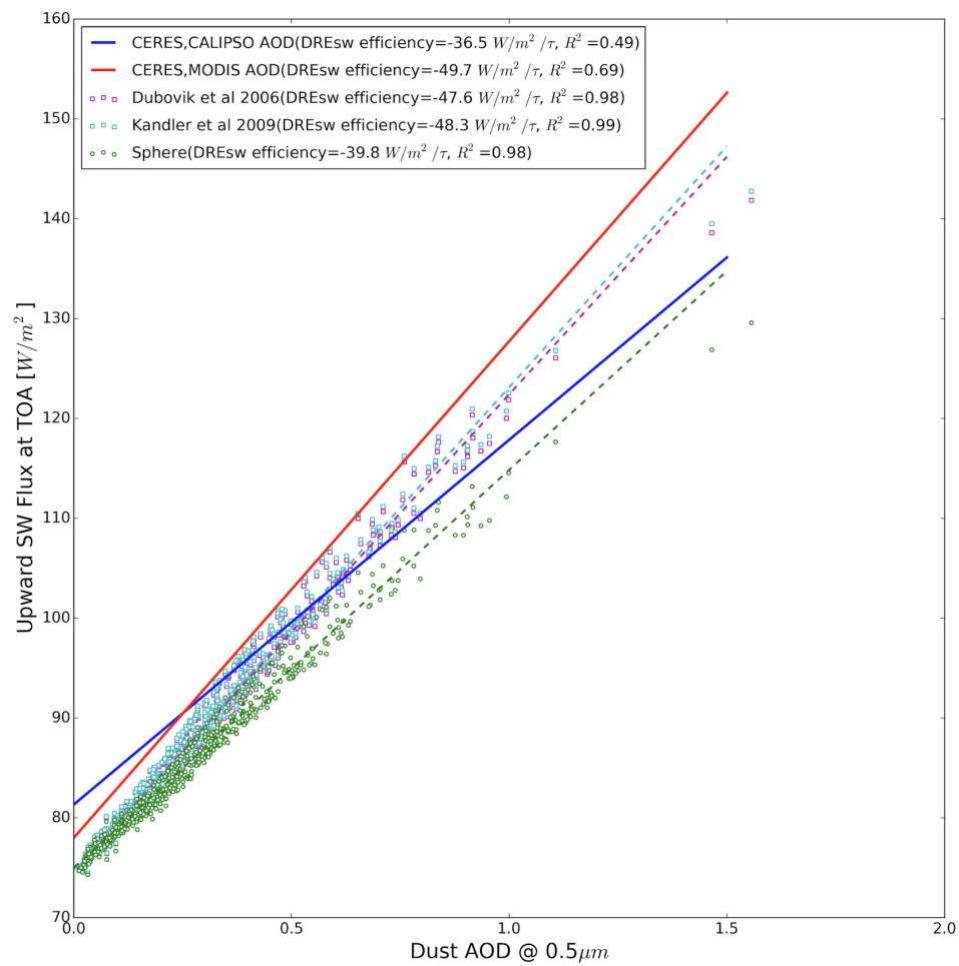890

891
892
893

894

895
896 *Figure 9* Extinction efficiency (Qe), b) single scattering albedo (SSA), c) asymmetry factor (g)
897 d) normalized AOD with respect to AOD @ 0.5 µm, and e) AOD*SSA*(1-g) of dust aerosols
898 based on different combination of PSD and refractive index. PSD type and refractive index type
899 are indicated in legends.

900

901
902
903
904
905
906
907
908
909
910
911
912

913

914
915
916 *Figure 10 shows the radiative transfer simulations for the selected cases based on the three dust*
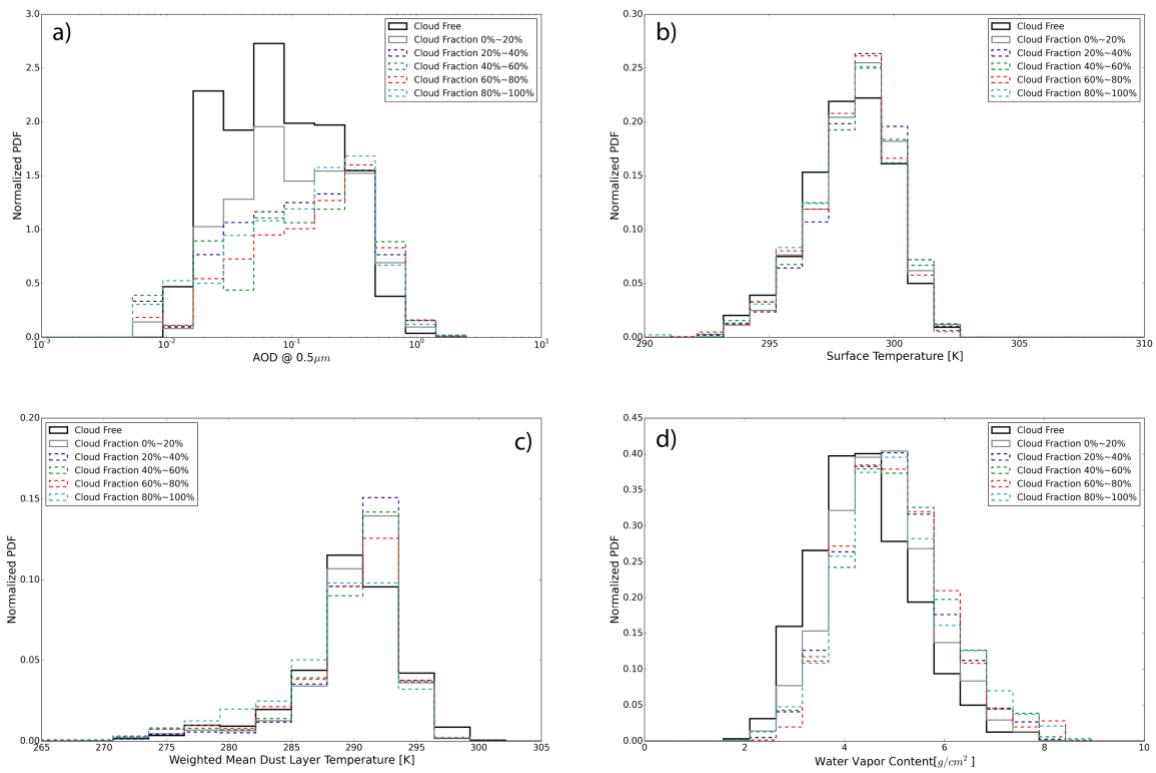917 *shape models.*

918
919
920
921
922

923
924 *Figure 11 Histograms of a) dust AOD, b) surface temperature c) dust temperature and d) total*
925 *column water vapor of dust dominant CERES pixels with different cloud fractions.*

926
927

928
929
930

References:

Ackerman, A. S., Toon, O. B., Stevens, D. E., et al., "Reduction of tropical cloudiness by soot", Science, **288**, 5468, 1042-1047, (2000), doi:DOI 10.1126/science.288.5468.1042.

Ackerman, S. A., Strabala, K. I., Menzel, W. P., et al., "Discriminating clear sky from clouds with MODIS", Journal of Geophysical Research-Atmospheres, **103**, D24, 32141-32157, (1998), doi:Doi 10.1029/1998jd200032.

Albrecht, B. A., "Aerosols, Cloud Microphysics, and Fractional Cloudiness", Science, **245**, 4923, 1227-1230, (1989), doi:DOI 10.1126/science.245.4923.1227.

Balkanski, Y., Schulz, M., Claquin, T. and Guibert, S., "Reevaluation of Mineral aerosol radiative forcings suggests a better agreement with satellite and AERONET data", Atmospheric Chemistry and Physics, **7**, 81-95, (2007), doi:DOI 10.5194/acp-7-81-2007.

Boucher, O., D. Randall, P. Artaxo, C. Bretherton, G. Feingold, P. Forster, V.-M. Kerminen, Y. Kondo, H. Liao, U. Lohmann, P. Rasch, S.K. Satheesh, S. Sherwood, B. Stevens and X.Y. Zhang, 2013: Clouds and Aerosols. In: Climate Change 2013: The Physical Science Basis. Contribution of Working Group I to the Fifth Assessment Report of the Intergovernmental Panel on Climate Change [Stocker, T.F., D. Qin, G.-K. Plattner, M. Tignor, S.K. Allen, J. Boschung, A. Nauels, Y. Xia, V. Bex and P.M. Midgley (eds.)]. Cambridge University Press, Cambridge, United Kingdom and New York, NY, USA.

Carlson, T. N. and Benjamin, S. G., "Radiative Heating Rates for Saharan Dust", Journal of the Atmospheric Sciences, **37**, 1, 193-213, (1980), doi:Doi 10.1175/1520-0469(1980)037<0193:Rhrfsd>2.0.Co;2.

Cess, R. D., "Nuclear-War - Illustrative Effects of Atmospheric Smoke and Dust Upon Solar-Radiation", Climatic Change, **7**, 2, 237-251, (1985), doi:Doi 10.1007/Bf00140508.

Choobari, O. A., P. Zawar-Reza and Sturman, A., "The global distribution of mineral dust and its impacts on the climate system: A review", Atmospheric Research, **138**, 152-165, (2014), doi:10.1016/j.atmosres.2013.11.007.

Colarco, P. R., Nowottnick, E. P., Randles, C. A., et al., "Impact of radiatively interactive dust aerosols in the NASA GEOS-5 climate model: Sensitivity to dust particle shape and refractive index", Journal of Geophysical Research-Atmospheres, **119**, 2, 753-786, (2014), doi:10.1002/2013jd020046.

Colarco, P. R., Toon, O. B., Torres, O. and Rasch, P. J., "Determining the UV imaginary index of refraction of Saharan dust particles from Total Ozone Mapping Spectrometer data using a three-dimensional model of dust transport", Journal of Geophysical Research-Atmospheres, **107**, D16, (2002), doi:Artn 4289 10.1029/2001jd000903.

Collins, W. D., Rasch, P. J., Eaton, B. E., et al., "Simulating aerosols using a chemical transport model with assimilation of satellite aerosol retrievals: Methodology for INDOEX", Journal of Geophysical Research-Atmospheres, **106**, D7, 7313-7336, (2001), doi:Doi 10.1029/2000jd900507.

Cuesta, J., Marsham, J. H., Parker, D. J. and Flamant, C., "Dynamical mechanisms controlling the vertical redistribution of dust and the thermodynamic structure of the West Saharan atmospheric boundary layer during summer", Atmospheric Science Letters, **10**, 1, 34-42, (2009), doi:10.1002/asl.207.

973 DeSouza-Machado, S. G., Strow, L. L., Hannon, S. E. and Motteler, H. E., "Infrared dust
974   spectral signatures from AIRS", Geophysical Research Letters, **33**, 3, (2006), doi:Artn
975   L03801
976 10.1029/2005gl024364.
977 Di Biagio, C., Formenti, P., Balkanski, Y., et al., "Global scale variability of the mineral dust
978   long-wave refractive index: a new dataset of in situ measurements for climate modeling
979   and remote sensing", Atmospheric Chemistry and Physics, **17**, 3, 1901-1929, (2017),
980   doi:10.5194/acp-17-1901-2017.
981 Di Biagio, C., Formenti, P., Styler, S. A., Pangui, E. and Doussin, J. F., "Laboratory chamber
982   measurements of the longwave extinction spectra and complex refractive indices of
983   African and Asian mineral dusts", Geophysical Research Letters, **41**, 17, 6289-6297,
984   (2014), doi:10.1002/2014gl060213.
985 Dubovik, O., Holben, B., Eck, T. F., et al., "Variability of absorption and optical properties of
986   key aerosol types observed in worldwide locations", Journal of the Atmospheric
987   Sciences, **59**, 3, 590-608, (2002), doi:Doi 10.1175/1520-
988   0469(2002)059<0590:Voaaop>2.0.Co;2.
989 Dubovik, O., Sinyuk, A., Lapyonok, T., et al., "Application of spheroid models to account for
990   aerosol particle nonsphericity in remote sensing of desert dust", Journal of Geophysical
991   Research-Atmospheres, **111**, D11, (2006), doi:Artn D11208 10.1029/2005jd006619.
992 Evan, A. T., Dunion, J., Foley, J. A., Heidinger, A. K. and Velden, C. S., "New evidence for a
993   relationship between Atlantic tropical cyclone activity and African dust outbreaks",
994   Geophysical Research Letters, **33**, 19, (2006), doi:Artn L19813 10.1029/2006gl026408.
995 Formenti, P., Schutz, L., Balkanski, Y., et al., "Recent progress in understanding physical and
996   chemical properties of African and Asian mineral dust", Atmospheric Chemistry and
997   Physics, **11**, 16, 8231-8256, (2011), doi:10.5194/acp-11-8231-2011.
998 Fouquart, Y., Bonnel, B., Brogniez, G., et al., "Observations of Saharan Aerosols - Results of
999   Eclats Field Experiment .2. Broad-Band Radiative Characteristics of the Aerosols and
1000   Vertical Radiative Flux Divergence", Journal of Climate and Applied Meteorology, **26**, 1,
1001   38-52, (1987), doi:10.1175/1520-0450(1987)026<0038:Oosaro>2.0.Co;2.
1002 Hansen, J., Sato, M. and Ruedy, R., "Radiative forcing and climate response", Journal of
1003   Geophysical Research-Atmospheres, **102**, D6, 6831-6864, (1997), doi:Doi
1004   10.1029/96jd03436.
1005 Hess, M., Koepke, P. and Schult, I., "Optical properties of aerosols and clouds: The software
1006   package OPAC", Bulletin of the American Meteorological Society, **79**, 5, 831-844,
1007   (1998), doi:Doi 10.1175/1520-0477(1998)079<0831:Opoaac>2.0.Co;2.
1008 Holz, R. E., Ackerman, S. A., Nagle, F. W., et al., "Global Moderate Resolution Imaging
1009   Spectroradiometer (MODIS) cloud detection and height evaluation using CALIOP",
1010   Journal of Geophysical Research-Atmospheres, **113**, (2008), doi:Artn D00a19
1011   10.1029/2008jd009837.
1012 Hsu, N. C., Herman, J. R. and Weaver, C., "Determination of radiative forcing of Saharan dust
1013   using combined TOMS and ERBE data", Journal of Geophysical Research-Atmospheres,
1014   **105**, D16, 20649-20661, (2000), doi:Doi 10.1029/2000jd900150.
1015 Jickells, T. D., An, Z. S., Andersen, K. K., et al., "Global iron connections between desert dust,
1016   ocean biogeochemistry, and climate", Science, **308**, 5718, 67-71, (2005), doi:DOI
1017   10.1126/science.1105959.

Kandler, K., Schutz, L., Deutscher, C., et al., "Size distribution, mass concentration, chemical and mineralogical composition and derived optical parameters of the boundary layer aerosol at Tinfou, Morocco, during SAMUM 2006", Tellus Series B-Chemical and Physical Meteorology, **61**, 1, 32-50, (2009), doi:10.1111/j.1600-0889.2008.00385.x.

Karyampudi, V. M., Palm, S. P., Reagen, J. A., et al., "Validation of the Saharan dust plume conceptual model using lidar, Meteosat, and ECMWF data", Bulletin of the American Meteorological Society, **80**, 6, 1045-1075, (1999), doi:Doi 10.1175/1520-0477(1999)080<1045:Votsdp>2.0.Co;2.

Kato, S., Rose, F. G., Sun-Mack, S., et al., "Improvements of top-of-atmosphere and surface irradiance computations with CALIPSO-, CloudSat-, and MODIS-derived cloud and aerosol properties", Journal of Geophysical Research-Atmospheres, **116**, (2011), doi:Artn D19209 10.1029/2011jd016050.

Kato, S., Sun-Mack, S., Miller, W. F., et al., "Relationships among cloud occurrence frequency, overlap, and effective thickness derived from CALIPSO and CloudSat merged cloud vertical profiles", Journal of Geophysical Research-Atmospheres, **115**, (2010), doi:Artn D00h28 10.1029/2009jd012277.

Keil, A. and Haywood, J. M., "Solar radiative forcing by biomass burning aerosol particles during SAFARI 2000: A case study based on measured aerosol and cloud properties", Journal of Geophysical Research-Atmospheres, **108**, D13, (2003), doi:Artn 8467 10.1029/2002jhd002315.

Kim, M. H., Kim, S. W., Yoon, S. C. and Omar, A. H., "Comparison of aerosol optical depth between CALIOP and MODIS-Aqua for CALIOP aerosol subtypes over the ocean", Journal of Geophysical Research-Atmospheres, **118**, 23, 13241-13252, (2013), doi:10.1002/2013jd019527.

Koepke, P., Gasteiger, J. and Hess, M., "Technical Note: Optical properties of desert aerosol with non-spherical mineral particles: data incorporated to OPAC", Atmospheric Chemistry and Physics, **15**, 10, 5947-5956, (2015), doi:10.5194/acp-15-5947-2015.

Kok, J. F., Ridley, D. A., Zhou, Q., et al., "Smaller desert dust cooling effect estimated from analysis of dust size and abundance", Nature Geoscience, **10**, 4, 274-+, (2017), doi:10.1038/Ngeo2912.

Koren, I., Kaufman, Y. J., Remer, L. A. and Martins, J. V., "Measurement of the effect of Amazon smoke on inhibition of cloud formation", Science, **303**, 5662, 1342-1345, (2004), doi:DOI 10.1126/science.1089424.

Lau, K. M. and Kim, K. M., "Cooling of the Atlantic by Saharan dust", Geophysical Research Letters, **34**, 23, (2007), doi:Artn L23811 10.1029/2007gl031538.

Levoni, C., Cervino, M., Guzzi, R. and Torricella, F., "Atmospheric aerosol optical properties: a database of radiative characteristics for different components and classes", Applied Optics, **36**, 30, 8031-8041, (1997), doi:Doi 10.1364/Ao.36.008031.

Levy, R. C., Remer, L. A., Mattoo, S., Vermote, E. F. and Kaufman, Y. J., "Second-generation operational algorithm: Retrieval of aerosol properties over land from inversion of Moderate Resolution Imaging Spectroradiometer spectral reflectance", Journal of Geophysical Research-Atmospheres, **112**, D13, (2007), doi:Artn D13211 10.1029/2006jd007811.

Li, F., Vogelmann, A. M. and Ramanathan, V., "Saharan dust aerosol radiative forcing measured from space", Journal of Climate, **17**, 13, 2558-2571, (2004), doi:Doi 10.1175/1520-0442(2004)017<2558:Sdarfm>2.0.Co;2.

1064 Liao, H. and Seinfeld, J. H., "Radiative forcing by mineral dust aerosols: sensitivity to key
1065   variables", Journal of Geophysical Research-Atmospheres, **103**, D24, 31637-31645,
1066   (1998), doi:10.1029/1998jd200036.
1067 Liu, Z. Y., Omar, A., Vaughan, M., et al., "CALIPSO lidar observations of the optical properties
1068   of Saharan dust: A case study of long-range transport", Journal of Geophysical Research-
1069   Atmospheres, **113**, D7, (2008), doi:Artn D07207 10.1029/2007jd008878.
1070 Ma, X., Bartlett, K., Harmon, K. and Yu, F., "Comparison of AOD between CALIPSO and
1071   MODIS: significant differences over major dust and biomass burning regions",
1072   Atmospheric Measurement Techniques, **6**, 9, 2391-2401, (2013), doi:10.5194/amt-6-
1073   2391-2013.
1074 Mahowald, N., Albani, S., Kok, J. F., et al., "The size distribution of desert dust aerosols and its
1075   impact on the Earth system", Aeolian Research, **15**, 53-71, (2014),
1076   doi:10.1016/j.aeolia.2013.09.002.
1077 Maring, H., Savoie, D. L., Izaguirre, M. A., Custals, L. and Reid, J. S., "Mineral dust aerosol size
1078   distribution change during atmospheric transport", Journal of Geophysical Research-
1079   Atmospheres, **108**, D19, (2003), doi:Artn 8592 10.1029/2002jd002536.
1080 McCormick, R. A. and Ludwig, J. H., "Climate Modification by Atmospheric Aerosols",
1081   Science, **156**, 3780, 1358-+, (1967), doi:DOI 10.1126/science.156.3780.1358.
1082 Meng, Z. K., Yang, P., Kattawar, G. W., et al., "Single-scattering properties of tri-axial
1083   ellipsoidal mineral dust aerosols: A database for application to radiative transfer
1084   calculations", Journal of Aerosol Science, **41**, 5, 501-512, (2010),
1085   doi:10.1016/j.jaerosci.2010.02.008.
1086 Miller, R. L. and Tegen, I., "Climate response to soil dust aerosols", Journal of Climate, **11**, 12,
1087   3247-3267, (1998), doi:Doi 10.1175/1520-0442(1998)011<3247:Crtsda>2.0.Co;2.
1088 Mishchenko, M. I., Travis, L. D., Kahn, R. A. and West, R. A., "Modeling phase functions for
1089   dustlike tropospheric aerosols using a shape mixture of randomly oriented polydisperse
1090   spheroids", Journal of Geophysical Research-Atmospheres, **102**, D14, 16831-16847,
1091   (1997), doi:Doi 10.1029/96jd02110.
1092 Mishra, M. K., Gupta, A. K. and Rajeev, K., "Spaceborne Observations of the Diurnal Variation
1093   of Shortwave Aerosol Direct Radiative Effect at Top of Atmosphere Over the Dust-
1094   Dominated Arabian Sea and the Atlantic Ocean", Ieee Transactions on Geoscience and
1095   Remote Sensing, **55**, 11, 6610-6616, (2017), doi:10.1109/Tgrs.2017.2730758.
1096 Mlawer, E. J., Taubman, S. J., Brown, P. D., Iacono, M. J. and Clough, S. A., "Radiative transfer
1097   for inhomogeneous atmospheres: RRTM, a validated correlated-k model for the
1098   longwave", Journal of Geophysical Research-Atmospheres, **102**, D14, 16663-16682,
1099   (1997), doi:Doi 10.1029/97jd00237.
1100 Myhre, G., Grini, A., Haywood, J. M., et al., "Modeling the radiative impact of mineral dust
1101   during the Saharan Dust Experiment (SHADE) campaign", Journal of Geophysical
1102   Research-Atmospheres, **108**, D18, (2003), doi:Artn 8579 10.1029/2002jd002566.
1103 Peyridieu, S., Chedin, A., Tanre, D., et al., "Saharan dust infrared optical depth and altitude
1104   retrieved from AIRS: a focus over North Atlantic - comparison to MODIS and
1105   CALIPSO", Atmospheric Chemistry and Physics, **10**, 4, 1953-1967, (2010),
1106   doi:10.5194/acp-10-1953-2010.
1107 Pierangelo, C., Chedin, A., Heilliette, S., Jacquinet-Husson, N. and Armante, R., "Dust altitude
1108   and infrared optical depth from AIRS", Atmospheric Chemistry and Physics, **4**, 1813-
1109   1822, (2004), doi:10.5194/acp-4-1813-2004.

1110   Platnick, S., King, M. D., Ackerman, S. A., et al., "The MODIS cloud products: Algorithms and
1111   examples from Terra", Ieee Transactions on Geoscience and Remote Sensing, **41**, 2, 459-
1112   473, (2003), doi:10.1109/Tgrs.2002.808301.
1113   Rajot, J. L., Formenti, P., Alfaro, S., et al., "AMMA dust experiment: An overview of
1114   measurements performed during the dry season special observation period (SOP0) at the
1115   Banizoumbou (Niger) supersite", Journal of Geophysical Research-Atmospheres, **113**,
1116   D20, (2008), doi:Artn D00c14 10.1029/2008jd009906.
1117   Ramaswamy, V. and Kiehl, J. T., "Sensitivies of the Radiative Forcing Due to Large Loadings
1118   of Smoke and Dust Aerosols", Journal of Geophysical Research-Atmospheres, **90**, Nd3,
1119   5597-5613, (1985), doi:DOI 10.1029/JD090iD03p05597.
1120   Remer, L. A., Kaufman, Y. J., Tanre, D., et al., "The MODIS aerosol algorithm, products, and
1121   validation", Journal of the Atmospheric Sciences, **62**, 4, 947-973, (2005), doi:Doi
1122   10.1175/Jas3385.1.
1123   Rienecker, M. M., Suarez, M. J., Todling, R., et al., " The GEOS-5 data assimilation system -
1124   Documentation of versions 5.0.1, 5.1.0, and 5.2.0", NASA Tech. Memo., **27**, (2008).
1125   Rosenfeld, D. and Lensky, I. M., "Satellite-based insights into precipitation formation processes
1126   in continental and maritime convective clouds", Bulletin of the American Meteorological
1127   Society, **79**, 11, 2457-2476, (1998), doi:Doi 10.1175/1520-
1128   0477(1998)079<2457:Sbiipf>2.0.Co;2.
1129   Ryder, C. L., Highwood, E. J., Lai, T. M., Sodemann, H. and Marsham, J. H., "Impact of
1130   atmospheric transport on the evolution of microphysical and optical properties of Saharan
1131   dust", Geophysical Research Letters, **40**, 10, 2433-2438, (2013a), doi:10.1002/grl.50482.
1132   Ryder, C. L., Highwood, E. J., Rosenberg, P. D., et al., "Optical properties of Saharan dust
1133   aerosol and contribution from the coarse mode as measured during the Fennec 2011
1134   aircraft campaign", Atmospheric Chemistry and Physics, **13**, 1, 303-325, (2013b),
1135   doi:10.5194/acp-13-303-2013.
1136   Sokolik, I. N. and Toon, O. B., "Direct radiative forcing by anthropogenic airborne mineral
1137   aerosols", Nature, **381**, 6584, 681-683, (1996), doi:DOI 10.1038/381681a0.
1138   Sokolik, I. N. and Toon, O. B., "Incorporation of mineralogical composition into models of the
1139   radiative properties of mineral aerosol from UV to IR wavelengths", Journal of
1140   Geophysical Research-Atmospheres, **104**, D8, 9423-9444, (1999), doi:Doi
1141   10.1029/1998jd200048.
1142   Sokolik, I. N., Toon, O. B. and Bergstrom, R. W., "Modeling the radiative characteristics of
1143   airborne mineral aerosols at infrared wavelengths", Journal of Geophysical Research-
1144   Atmospheres, **103**, D8, 8813-8826, (1998), doi:Doi 10.1029/98jd00049.
1145   Stegmann, P. G. and Yang, P., "A regional, size-dependent, and causal effective medium model
1146   for Asian and Saharan mineral dust refractive index spectra", Journal of Aerosol Science,
1147   **114**, 327-341, (2017), doi:10.1016/j.jaerosci.2017.10.003.
1148   Tegen, I. and Lacis, A. A., "Modeling of particle size distribution and its influence on the
1149   radiative properties of mineral dust aerosol", Journal of Geophysical Research-
1150   Atmospheres, **101**, D14, 19237-19244, (1996), doi:Doi 10.1029/95jd03610.
1151   Tegen, I., Lacis, A. A. and Fung, I., "The influence on climate forcing of mineral aerosols from
1152   disturbed soils", Nature, **380**, 6573, 419-422, (1996), doi:10.1038/380419a0.
1153   Textor, C., Schulz, M., Guibert, S., et al., "Analysis and quantification of the diversities of
1154   aerosol life cycles within AeroCom", Atmospheric Chemistry and Physics, **6**, 1777-1813,
1155   (2006).

Twomey, S., "The influence of pollution on the shortwave albedo of clouds", Journal of the atmospheric sciences, **34**, 7, 1149-1152, (1977).

Volz, F. E., "Infrared Optical-Constants of Ammonium Sulfate, Sahara Dust, Volcanic Pumice, and Flyash", Applied Optics, **12**, 3, 564-568, (1973), doi:10.1364/Ao.12.000564.

Volz, F. E., "Infrared Refractive-Index of Atmospheric Aerosol Substances", Applied Optics, **11**, 4, 755-759, (1972), doi:Doi 10.1364/Ao.11.000755.

Washington, R., Todd, M., Middleton, N. J. and Goudie, A. S., "Dust-storm source areas determined by the total ozone monitoring spectrometer and surface observations", Annals of the Association of American Geographers, **93**, 2, 297-313, (2003), doi:Doi 10.1111/1467-8306.9302003.

Weinzierl, B., Ansmann, A., Prospero, J. M., et al., "THE SAHARAN AEROSOL LONG-RANGE TRANSPORT AND AEROSOL-CLOUD-INTERACTION EXPERIMENT Overview and Selected Highlights", Bulletin of the American Meteorological Society, **98**, 7, 1427-1451, (2017), doi:10.1175/Bams-D-15-00142.1.

Weinzierl, B., Sauer, D., Esselborn, M., et al., "Microphysical and optical properties of dust and tropical biomass burning aerosol layers in the Cape Verde region-an overview of the airborne in situ and lidar measurements during SAMUM-2", Tellus Series B-Chemical and Physical Meteorology, **63**, 4, 589-618, (2011), doi:10.1111/j.1600-0889.2011.00566.x.

Winker, D. M., Pelon, J., Coakley, J. A., et al., "THE CALIPSO MISSION A Global 3D View of Aerosols and Clouds", Bulletin of the American Meteorological Society, **91**, 9, 1211-1229, (2010), doi:10.1175/2010bams3009.1.

Wiscombe, W. J., "Improved Mie Scattering Algorithms", Applied Optics, **19**, 9, 1505-1509, (1980), doi:Doi 10.1364/Ao.19.001505.

Xu, H., Guo, J. P., Wang, Y., et al., "Warming effect of dust aerosols modulated by overlapping clouds below", Atmospheric Environment, **166**, 393-402, (2017), doi:10.1016/j.atmosenv.2017.07.036.

Yang, E. S., Gupta, P. and Christopher, S. A., "Net radiative effect of dust aerosols from satellite measurements over Sahara", Geophysical Research Letters, **36**, (2009), doi:Artn L18812 10.1029/2009gl039801.

Yu, H., Kaufman, Y. J., Chin, M., et al., "A review of measurement-based assessments of the aerosol direct radiative effect and forcing", Atmospheric Chemistry and Physics, **6**, 613-666, (2006).

Yu, H. B., Chin, M., Yuan, T. L., et al., "The fertilizing role of African dust in the Amazon rainforest: A first multiyear assessment based on data from Cloud-Aerosol Lidar and Infrared Pathfinder Satellite Observations", Geophysical Research Letters, **42**, 6, 1984-1991, (2015), doi:10.1002/2015gl063040.

Zhang, Z. B., Meyer, K., Yu, H. B., et al., "Shortwave direct radiative effects of above-cloud aerosols over global oceans derived from 8 years of CALIOP and MODIS observations", Atmospheric Chemistry and Physics, **16**, 5, 2877-2900, (2016), doi:10.5194/acp-16-2877-2016.

Zhou, M., Yu, H., Dickinson, R. E., Dubovik, O. and Holben, B. N., "A normalized description of the direct effect of key aerosol types on solar radiation as estimated from Aerosol Robotic Network aerosols and Moderate Resolution Imaging Spectroradiometer albedos", Journal of Geophysical Research-Atmospheres, **110**, D19, (2005), doi:Artn D19202 10.1029/2005jd005909.

1202
1203
1204